J. Plasma Phys. (2026), *vol*. 92, E20 © The Author(s), 2026. Published by Cambridge University Press.
This is an Open Access article, distributed under the terms of the Creative Commons Attribution licence (https://creativecommons.org/licenses/by/4.0/), which permits unrestricted re-use, distribution and reproduction, provided the original article is properly cited. doi:10.1017/S002237782510113X

Role of ion acoustic instability in magnetic reconnection

Dion Li[1], **Zhuo Liu**[1] and **Nuno F. Loureiro**[1]

[1]Plasma Science and Fusion Center, Massachusetts Institute of Technology, Cambridge, MA 02139, USA

Corresponding author: Dion Li, dionli@psfc.mit.edu

(Received 14 May 2025; revision received 29 October 2025; accepted 25 November 2025)

We report on a first-principles numerical study of magnetic reconnection in plasmas with different initial ion-to-electron temperature ratios. In cases where this ratio is significantly below unity, we observe intense wave activity in the diffusion region, driven by the ion-acoustic instability. Our analysis shows that the dominant macroscopic effect of this instability is to drive substantial ion heating. In contrast to earlier studies reporting significant anomalous resistivity, we find that anomalous contributions due to the ion-acoustic instability are minimal. These results shed light on the dynamical impact of this instability on reconnection processes, offering new insights into the fundamental physics governing collisionless reconnection.

Key words: plasma instabilities, space plasma physics, plasma simulation

1. Introduction

Magnetic reconnection is a phenomenon in which the topology of the magnetic field in a plasma is rearranged and magnetic energy is converted into kinetic or thermal energy (Yamada, Kulsrud & Ji 2010; Ji *et al*. 2022). Reconnection has been widely observed and has broad applications in space plasma events, such as solar flares (Forbes 1991) and coronal mass ejections (Gosling, Birn & Hesse 1995), the Earth's and planetary magnetospheres (Chen *et al*. 2008; Slavin *et al*. 2009; Le *et al*. 2017; Phan *et al*. 2018; Hesse & Cassak 2020), and in a wide variety of astrophysical and laboratory settings (Yamada *et al*. 1994, 2010; Uzdensky 2011; Hare *et al*. 2018).

In the realm of collisionless reconnection, a persistent challenge has been to pinpoint the kinetic processes that facilitate rapid topological changes and energy conversion. Specifically, kinetic instabilities have been proposed to play an important role. These instabilities, through intense wave–particle interactions, may generate anomalous resistivity (Sagdeev 1967; Galeev & Sagdeev 1983; Labelle & Treumann 1988; Treumann 2014; Liu *et al*. 2024) and could determine the reconnection rate (Ji *et al*. 1998; Kulsrud 1998, 2014; Uzdensky 2003; Treumann 2014). Observational evidence (Carter *et al*. 2001; Deng & Matsumoto 2001; Farrell *et al*. 2002; Matsumoto *et al*. 2003; Eastwood *et al*. 2009; Laitinen *et al*. 2010;

https://doi.org/10.1017/S002237782510113X Published online by Cambridge University Press

Graham *et al*. 2017, 2019; Khotyaintsev *et al*. 2019; Chen *et al*. 2020; Yoo *et al*. 2020; Wang *et al*. 2022; Cozzani *et al*. 2023) and numerical simulations (Daughton 2003; Drake *et al*. 2003; Daughton, Lapenta & Ricci 2004; Roytershteyn *et al*. 2012; Fujimoto 2014; Jara-Almonte, Daughton & Ji 2014; Le *et al*. 2018; Dokgo *et al*. 2019; Le *et al*. 2019; Ng *et al*. 2020*a*; Wang *et al*. 2021; Yi *et al*. 2023; Zhang *et al*. 2023) confirm the presence of turbulent phenomena and wave emissions in the vicinity of diffusion regions at reconnection sites, indicating that these instabilities are active players in reconnection dynamics. Moreover, they might affect the onset of reconnection itself (Ricci *et al*. 2004; Alt & Kunz 2019; Winarto & Kunz 2022).

Among the various potential kinetic modes, the ion-acoustic instability (IAI), driven by the relative drift between ions and electrons (or the electric current), has been proposed as a key factor in the dissipation of magnetic energy in collisionless plasmas (Coppi & Friedland 1971; Smith & Priest 1972; Coroniti & Eviatar 1977; Sagdeev 1979) and appears to be a compelling explanation for numerous observations of ion-acoustic waves (IAWs) across different plasma settings. As far back as the 1970s, the Helios I and II missions have documented the presence of IAWs within heliocentric distances ranging from 0.3 to 1 AU (Gurnett & Anderson 1977; Gurnett & Frank 1978), setting the stage for renewed interest in the role of these waves in the solar wind. More recently, advanced instrumentation from NASA's Parker Solar Probe (PSP) (Fox *et al*. 2015) and the European Space Agency's Solar Orbiter (Müller *et al*. 2012) has further highlighted the prominence of IAWs in the near-Sun environment. For example, the Solar Orbiter's Time Domain Sampler receiver reveals that IAWs are a dominant wave mode close to the Sun (Graham *et al*. 2021; Píša *et al*. 2021), underscoring their importance for solar and heliospheric physics.

Observations of these waveforms may shed light on a longstanding question in solar physics: why proton temperatures in the solar wind decline much more slowly than predicted by simple adiabatic expansion, especially at distances beyond 20 AU (Bridge *et al*. 1977; Richardson & Smith 2003; Mozer *et al*. 2023). This discrepancy implies the presence of additional heating mechanisms, possibly due to the turbulent nature of the solar wind (Tu & Marsch 1995; Bruno & Carbone 2005). In particular, turbulence can drive localised magnetic reconnection events (Retinò *et al*. 2007; Servidio *et al*. 2009, 2011; Osman *et al*. 2014; Loureiro & Boldyrev 2017) in the solar wind, with associated large currents. The existence of solar wind patches where ions are noticeably colder than electrons (Hellinger *et al*. 2013; Štverák *et al*. 2015; Chen 2016; Verscharen, Klein & Maruca 2019; Píša *et al*. 2021) suggests that IAI can potentially be triggered in such events. Recent studies (Liu *et al*. 2024) and our own findings in this paper suggest that IAI can efficiently heat ions, providing a plausible explanation (among others) for the persistent, but not fully understood, ion heating in the solar wind over vast distances.

In this investigation, we focus specifically on the role of IAI in a simple, two-dimensional reconnecting configuration to determine whether it can provide a viable pathway for ion heating and wave generation within collisionless reconnection. Through a series of high-fidelity particle-in-cell numerical simulations, we find that this is indeed the case when the initial ion temperature is significantly lower than that of the electrons.

This paper is organised as follows. § 2 outlines the theoretical framework of IAI, highlighting its relevance to magnetic reconnection. § 3 describes the particle-in-cell simulation set-up and parameters. § 4 presents the results, including the reconnection rate (§ 4.1), conditions for IAI emergence (§ 4.2), evidence of IAW generation (§ 4.3)

https://doi.org/10.1017/S002237782510113X Published online by Cambridge University Press

and the role of IAI in reconnection dynamics (§ 4.4). Finally, § 5 discusses the implications of these findings on ion heating in the solar wind and suggests directions for future research.

2. Theoretical framework

In this section, we revisit the IAI derivation by examining the wave mode solution parallel to the electron–ion drift. For non-relativistic systems, the Vlasov–Poisson equations are expressed as

$$\frac{\partial f_\alpha}{\partial t} + \boldsymbol{v}\cdot\nabla f_\alpha + \left(-\frac{q_\alpha}{m_\alpha}\nabla\varphi\right)\cdot\frac{\partial f_\alpha}{\partial \boldsymbol{v}} = 0, \tag{2.1}$$

$$\nabla^2\varphi = -4\pi\sum_\alpha q_\alpha\int \mathrm{d}^3v\, f_\alpha, \tag{2.2}$$

with $\alpha = i, e$ the particle species index. The combined and linearised equations for the $1+1$-dimensional (x, v_x) case can be expressed in the form of a dielectric function

$$\epsilon(p,k) = 1 - \sum_\alpha \frac{\omega_{p\alpha}^2}{k^2}\frac{1}{n_\alpha}\int \mathrm{d}v_x\, \frac{F'_\alpha(v_x)}{v_x - ip/k}, \tag{2.3}$$

where $\omega_{p\alpha}$ is the plasma frequency, $p \equiv -i\omega + \gamma$ and $F'_\alpha(v_x)$ is the derivative of the one-dimensional (1-D) velocity distribution function with respect to v_x. In the electrostatic scenario, the left-hand side of (2.3) is identically zero. By assuming both ion and electron species follow Maxwellian distributions, with electrons drifting at a speed U_d relative to the ions, (2.3) yields

$$1 + \frac{1+Z_p\left[(\omega-kU_d)/(\sqrt{2}kv_{\mathrm{th},e})\right]}{k^2\lambda_{De}^2} + \frac{1+Z_p\left[\omega/(\sqrt{2}kv_{\mathrm{th},i})\right]}{k^2\lambda_{Di}^2} + i\left\{\frac{Z_\Delta\left[(\omega-kU_d)/(\sqrt{2}kv_{\mathrm{th},e})\right]}{k^2\lambda_{De}^2} + \frac{Z_\Delta\left[\omega/(\sqrt{2}kv_{\mathrm{th},i})\right]}{k^2\lambda_{Di}^2}\right\} = 0, \tag{2.4}$$

where $v_{\mathrm{th},\alpha} = \sqrt{T_\alpha/m_\alpha}$ represents the thermal velocity, $\lambda_{D\alpha}$ the Debye length and we define

$$Z_p(\zeta) \equiv -\mathrm{erfi}(\zeta)Z_\Delta(\zeta), \tag{2.5}$$

$$Z_\Delta(\zeta) \equiv \sqrt{\pi}\zeta e^{-\zeta^2}, \tag{2.6}$$

and $\mathrm{erfi}(\zeta)$ the imaginary error function. In the numerical simulations that follow, we find that both ions and electrons approximately follow (drifting) Maxwellian distributions within the diffusion region when IAI begins to be triggered, that is, when the peak outflow electron–ion drift starts to exceed the ion-acoustic threshold drift (see, e.g. figure 3). As such, the assumption of (drifting) Maxwellians employed in (2.4) is justified.

Equation (2.4) can be solved numerically to obtain the growth rates and spectrum of IAWs. Notably, IAI is only triggered under specific conditions. For $T_i/T_e \ll 1$, a necessary criterion is that the electron–ion drift speed must be approximately or

https://doi.org/10.1017/S002237782510113X Published online by Cambridge University Press

larger than the ion-sound speed $c_s = \sqrt{(\gamma_e T_e + \gamma_i T_i)/m_i} \approx \sqrt{(T_e + 3T_i)/m_i}$,[1] where γ_α is the adiabatic index of species α , and we have assumed that electrons are isothermal ($\gamma_e = 1$) and ions are adiabatic ($\gamma_i = 3$) (Biskamp 2000).

In the context of collisionless magnetic reconnection, one may expect IAI to be driven in both the out-of-plane and in-plane directions. The out-of-plane direction is influenced by the reconnection current and the associated reconnection electric field, while the in-plane direction is driven by the current and electric field resulting from decoupled ion and electron flows in the outflow direction. The former mechanism was briefly addressed by Liu *et al*. (2024). The condition for the onset of out-of-plane IAI can be approximated as

$$\frac{J_z/en}{c_s} \sim \frac{cB_0}{4\pi\delta en}\sqrt{\frac{m_i}{T_e}} = \sqrt{\frac{2}{\beta_e}}\frac{d_i}{\delta} > 1, \tag{2.7}$$

where J_z is the out-of-plane current density, B_0 is the upstream (reconnecting) magnetic field, δ is the current sheet thickness, $d_i = c/\omega_{pi} = c(m_i/4\pi ne^2)^{1/2}$ is the ion inertial length or ion skin-depth and β_e is the electron plasma beta based on the reconnecting field. This condition is easy to satisfy since δ is expected to be of the order of the electron skin-depth.

Likewise, it is inevitable that the in-plane IAI will be triggered if $T_i/T_e \ll 1$ because the in-plane electron–ion drift should reach $U_{d,\text{in-plane}} \simeq v_{A,e} - v_{A,i}$, giving

$$\frac{U_{d,\text{in-plane}}}{c_s} \sim \frac{v_{A,e} - v_{A,i}}{c_s} \simeq \frac{v_{A,e}}{c_s} = \frac{B_0}{\sqrt{4\pi n_e m_e}}\sqrt{\frac{m_i}{T_e}} = \sqrt{\frac{m_i}{m_e}}\sqrt{\frac{2}{\beta_e}} \gg 1, \tag{2.8}$$

where $v_{A,\alpha} = B_0/(4\pi n_\alpha m_\alpha)^{1/2}$ is the Alfvén speed of species α. This result is illustrated in figure 1, which presents numerical solutions of the growth rate for the fastest growing wave mode and the wavenumber at which this maximum growth rate occurs, calculated by solving (2.4) using the initial thermal velocities from the simulations that follow and assuming uniform number densities $n_i = n_e = n_b = 0.2n_0$ (the approximate ion and electron density near the x-point around the time of peak reconnection rate in all simulations). The figure shows that there exists a range of drift speeds below the theoretical maximum of $U_d = v_{A,e} - v_{A,i}$ (identified by the purple vertical lines in figure 1[2]) for which the growth rate of the fastest growing mode is positive for all ion–electron temperature ratios considered. In the numerical simulations that follow, we find that the outflow electron–ion drift speed $|U_{d,\text{outflow}}| = |u_{x,e} - u_{xi}|$ reaches $\approx v_{A,e}/2$ at the outflow ends of the diffusion region, a result that is roughly independent of temperature ratio (see figures 4 and 3), which, alongside figure 1, suggests that IAI can be strongly triggered for $T_{i0}/T_{e0} = 1/10$ and $1/50$, but not for $T_{i0}/T_{e0} = 1$.

[1]For $T_i/T_e < 1/20$, the critical drift velocity for triggering IAI is actually $U_{d,\text{IAI}} \simeq 4\sqrt{2}v_{\text{th},i}$ (Fried & Gould 1961). Only at higher temperature ratios (e.g. $T_i/T_e > 1/10$) does this threshold become comparable to c_s (or larger than c_s as the temperature ratio approaches or exceeds unity). In our coldest-ion case, however, $T_{i0}/T_{e0} = 1/50$ and $4\sqrt{2}v_{\text{th},i}/c_s \simeq 4\sqrt{2}\sqrt{T_i/T_e} = 0.8 \sim 1$, which justifies the approximation that the threshold is $\sim c_s$.

[2]Notice the reason that these lines do not overlap in figure 1 is imposed by the requirements of the equilibrium set-up (see § 3), resulting in different $T_{e0} + 3T_{i0}$ (and hence, c_s) for different temperature ratios.

https://doi.org/10.1017/S002237782510113X Published online by Cambridge University Press

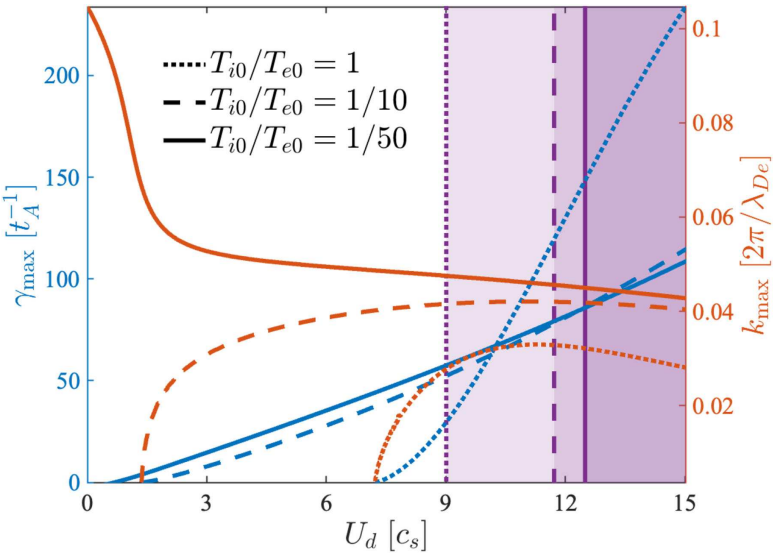

FIGURE 1. Maximum growth rates ($\gamma_{\max}$, in blue) and the corresponding wavenumbers ($k_{\max}$, in orange) as functions of drift velocity (U_d) for $T_{i0}/T_{e0} = 1$ (dotted lines), $T_{i0}/T_{e0} = 1/10$ (dashed lines) and $T_{i0}/T_{e0} = 1/50$ (solid lines). These values are obtained from solving (2.4), using the thermal velocities initialised in the simulations and $n_i = n_e = n_b = 0.2n_0$. Regions not accessible within the considered reconnection configuration along the outflow symmetry line are shaded in purple, with the purple lines representing the maximum expected electron–ion drift velocity ($U_{d,\text{in-plane}} = v_{A,e} - v_{A,i}$) at the ends of the diffusion region for each ion–electron temperature ratio. The increase in $k_{\max}$ at $\gamma_{\max} = 0$ as T_{i0}/T_{e0} decreases beyond $1/10$ is explained in Appendix A.

Due to computational constraints, this study considers only the two-dimensional case, with the out-of-plane and invariant direction aligned with $\hat{z}$, and focuses exclusively on the in-plane component of IAI.

3. Simulation set-up

The simulations reported in this work are conducted using the particle-in-cell (PIC) code osiris (Fonseca *et al*. 2002; Hemker 2015). The initial conditions are set to a Harris sheet equilibrium (Harris 1962), with the initial magnetic vector potential expressed as

$$\boldsymbol{A} = \hat{z} B_0 \lambda_{\mathrm{B}} \ln\left[\cosh\left(\frac{y}{\lambda_{\mathrm{B}}}\right)\right]. \tag{3.1}$$

Here, λ_{B} is the characteristic length scale of the magnetic field gradient (half-width of the current sheet). The initial density distribution is defined as

$$n_e = n_i = n_0 \mathrm{sech}^2\left(\frac{y}{\lambda_{\mathrm{B}}}\right) + n_b, \tag{3.2}$$

with $n_b = 0.2n_0$ the background number density.

The global Alfvén time is defined as $t_A = L_x/v_{A,i0}$, where L_x and L_y are the lengths of the simulation box in the x (outflow) and y (inflow) directions. The ion and

https://doi.org/10.1017/S002237782510113X Published online by Cambridge University Press

Parameter	Value
$8\pi n_0(T_{i0}+T_{e0})/B_0^2$	1
ω_{pe}/Ω_{ce}	2
m_i/m_e	100
L_x/d_{i0}	32
λ_B/d_{i0}	1
n_b/n_0	0.2
t_{max}/t_A	2.25
$\delta\psi/B_0d_{i0}$	0.1
Particles-per-cell	256 (16×16)

TABLE 1. Summary of simulation parameters.

T_{i0}/T_{e0}	1/50	1/10	1
L_y/d_{i0}	24	24	16
$\Delta x/\lambda_{De}=\Delta y/\lambda_{De}$	0.321	$\sim1/3$	$\sim1/3$
$\lambda_{De}/d_{e0}=u_{th,e}/c$	0.350	0.337	0.250
Resolution	2848×2136	2848×2136	3840×1920
Time step ($\omega_{pe}\Delta t$)	0.0786	0.0786	0.0583

TABLE 2. Simulation-specific parameters.

electron out-of-plane current densities are specified by $J_{zi0}/J_{ze0}=T_{i0}/T_{e0}$ to establish Vlasov equilibrium (Schindler 2006), with T_{i0} and T_{e0} uniform, and $\boldsymbol{J}_0=c(\boldsymbol{\nabla}\times\boldsymbol{B}_0/4\pi)$. The force-balance condition is satisfied by setting $n_0(T_{i0}+T_{e0})=B_0^2/8\pi$. The relationship between the electron plasma and cyclotron frequencies is given by $\omega_{pe}=2\Omega_{ce}$, where $\omega_{pe}=(4\pi n_0e^2/m_e)^{1/2}$ and $\Omega_{ce}=|e|B_0/(m_ec)$.

The initial perturbation is similar to that described by Daughton *et al.* (2009), with $\delta\boldsymbol{B}=\hat{\boldsymbol{z}}\times\boldsymbol{\nabla}\psi$ and $\psi=-\delta\psi\cos(2\pi x/L_x)\cos(\pi y/L_y)$, where the perturbation amplitude is set to $\delta\psi/B_0d_{i0}=0.1$. We use cubic particle interpolations and resolve the electron Debye length (λ_{De}) to prevent numerical heating. As a result, it was essential to adjust the resolution and time step parameters based on the ion–electron temperature ratio.

Key simulation parameters used in these runs are listed in tables 1 and 2.

4. Simulation results and wave activity in the diffusion region

In this section, we describe and analyse in detail the results of our numerical simulations. We begin with an overview of the reconnection dynamics observed across the simulations, emphasising the relatively minor impact of the temperature ratio on the reconnection rate. Despite this, significant wave activity is detected in the diffusion region, leading to pronounced ion heating. We argue in the following sections that this wave activity is driven by IAI, and characterise its onset and impact on reconnection dynamics.

https://doi.org/10.1017/S002237782510113X Published online by Cambridge University Press

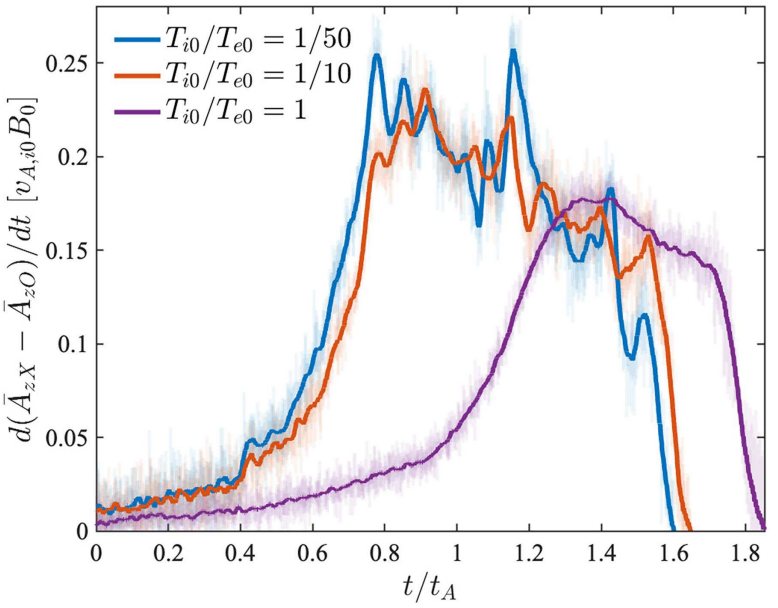

FIGURE 2. Time evolution of the temporally averaged reconnection rate for $T_{i0}/T_{e0} = 1/50$ (blue), $T_{i0}/T_{e0} = 1/10$ (orange) and $T_{i0}/T_{e0} = 1$ (purple). A_{zX} and A_{zO} are the out-of-plane magnetic vector potentials at the X and O points, respectively, and the semi-transparent curves are more exact values of the solid curves.

4.1. *Reconnection rate*

Plotted in figure 2 is the normalised reconnection rate (computed as the difference in the magnetic vector potential's rate of change at the X and O points, and temporally averaged over a moving window of $\approx 0.03\, t_A$) for each value of the ion–electron temperature ratio that we have numerically simulated. As shown, we find that the onset of fast reconnection occurs earlier in time for colder ions; however, the peak reconnection rate is weakly dependent on the temperature ratio – varying by less than a factor of 2 across values of T_{i0}/T_{e0} ranging from 1/50 to 1 – and is consistent with the established values in the literature (e.g. Birn *et al*. 2001; Cassak, Liu & Shay 2017). Also evident from the plot is the highly oscillatory nature of the curves corresponding to low initial temperature ratios during the fast reconnection stage, in contrast with the $T_{i0}/T_{e0} = 1$ case. This behaviour hints at turbulent dynamics in the current sheet during those times which, as we will demonstrate later, is due to the destabilisation of ion-acoustic modes.

4.2. *Onset of ion acoustic instability (IAI)*

We find that the outflow electron–ion drift speed $|U_{d,\mathrm{outflow}}|$ exceeds the IAI threshold drift in the diffusion region and near the separatrix for the cases $T_{i0}/T_{e0} = 1/50$ and 1/10. This is shown in figure 3, which illustrates the evolution of the outflow electron–ion drift along the outflow symmetry line ($y = 0$) near the x-point for the different temperature ratios considered, compared with the corresponding IAI threshold drift speeds (dashed lines; at times when the peak drifts begin to exceed the thresholds), calculated with local ion-acoustic speeds $c_s = \sqrt{(T_{e,xx} + 3T_{i,xx})/m_i}$. This drift occurs within the ion diffusion region because ions decouple from the magnetic

https://doi.org/10.1017/S002237782510113X Published online by Cambridge University Press

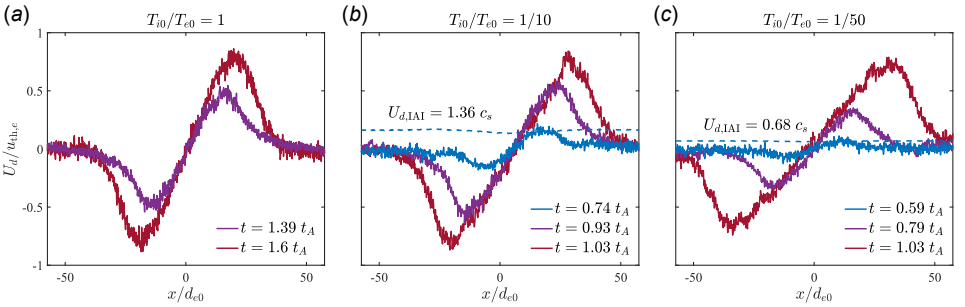

FIGURE 3. Evolution of the outflow electron–ion drift ($U_d = u_{x,e} - u_{x,i}$), normalised to the initial electron thermal velocity $u_{\mathrm{th},e}$, along the outflow symmetry line ($y = 0$) for (*a*) $T_{i0}/T_{e0} = 1$, (*b*) $T_{i0}/T_{e0} = 1/10$ and (*c*) $T_{i0}/T_{e0} = 1/50$. The blue curves denote the times when the drifts begin to exceed the corresponding IAI thresholds (which, for $T_{i0}/T_{e0} = 1$, never occurs and thus no blue curve is shown in panel *a*), the purple curves refer to the approximate times of peak reconnection rates and the red curves represent later times when the drifts reach maximum values. Dashed lines show the corresponding IAI threshold drift speeds (at times when the peak drifts begin to exceed the thresholds), calculated with local ion-acoustic speeds $c_s = \sqrt{(T_{e,xx} + 3T_{i,xx})/m_i}$.

field lines on electron scales, allowing for both ion and electron outflow speeds to approach their respective Alfvén speeds (Shay & Drake 1998; Liu *et al*. 2022).

The separation of electron and ion outflow velocities is illustrated in the phase-space distributions presented in figure 4 (see also figure 3 and the contours in figure 5), which shows ion and electron phase-space densities as functions of the particles' proper velocity and position in the outflow direction (u_x and x, respectively). Figure 4(*a,b*) also reveals nonlinear ion phase-space structures, which coincide with the emergence of waveforms in the diffusion region that, in the next subsection, we associate with IAWs.

Notably, figure 4 demonstrates that the maximum ion proper velocities (which are approximately ion bulk velocities due to the relatively low ion temperatures), attained at the end-points of the current sheet, closely match the Alfvén speed at those locations ($v_{A,i} \simeq 0.15 u_{\mathrm{th,e}}$), aligning with the established understanding of reconnection physics that the bulk plasma is accelerated to $v_{A,i}$ in the outflow direction. The maximum electron outflow velocity, which is $\approx 0.8 u_{\mathrm{th,e}} \approx v_{A,e}/2$ (see figure 3), being much larger than that of the ions implies that there is a large in-plane current.[3]

Figure 3 shows that that the electron–ion drifts begin to exceed the corresponding IAI thresholds (see figure 1, which gives $U_{d,\mathrm{IAI}}/c_s = U_d\ (\gamma_{\max} = 0)/c_s \approx 7.19$, 1.36 and 0.68 for $T_{i0}/T_{e0} = 1$, 1/10 and 1/50) at $t \approx 0.74\, t_A$ and $t \approx 0.59\, t_A$ for $T_{i0}/T_{e0} = 1/10$ and 1/50, respectively. These approximate times correlate well with the emergence of waveforms in the diffusion region (see figure 6 for the $T_{i0}/T_{e0} = 1/50$ case).

[3]We can analyse the development of the electron–ion drift in the diffusion region by calculating the expected proper velocity for each species at each x-position near the x-point using the formula $\langle u_{x,\alpha} \rangle = \int du_x\, u_x\, f_\alpha(x, y = 0, u_x) / \int du_x\, f_\alpha(x, y = 0, u_x)$. Here, u is used to calculate the drift instead of v because, formally, the vertical dimension of the phase-space distributions shown in figure 4 represents the proper velocity vectors $\boldsymbol{u} = \gamma_L \boldsymbol{v}$, with $\gamma_L = (1 - v^2/c^2)^{-1/2}$ the Lorentz factor. We observe that the electron proper velocity in the x-direction near the outflow edges can reach up to $u_{x,e} \simeq 0.7c$, corresponding to a Lorentz factor of $\gamma_L \simeq 1.22$. This value indicates that the motion is only mildly relativistic, thereby justifying the use of the non-relativistic Vlasov–Poisson equations (2.1) and (2.2) for interpreting the results.

https://doi.org/10.1017/S002237782510113X Published online by Cambridge University Press

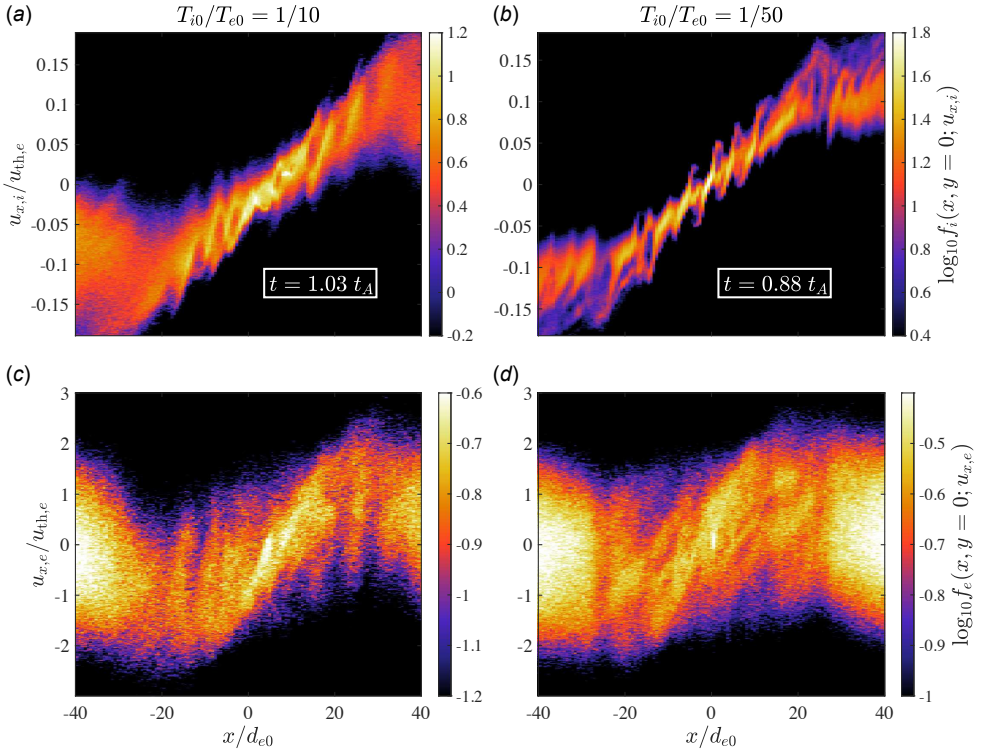

FIGURE 4. (*a,b*) Ion and (*c,d*) electron phase-space distributions in u_x and x along the outflow symmetry line ($y = 0$) near the x-point for (*a,c*) $T_{i0}/T_{e0} = 1/10$ and (*b,d*) $T_{i0}/T_{e0} = 1/50$ at the approximate times when IAI is strongly triggered.

We further demonstrate the decoupling between electron and ion drifts in figure 5, which displays colourmaps of the outflow electron–ion drift velocity along with contours highlighting where this drift exceeds the associated IAI threshold drift. Additionally, it depicts the magnitude of the outflow electric field (E_x), whose wave-like structures we examine in detail in the next section.

4.3. *Identification of IAWs*

A salient feature in the contour plots of figure 5 is the appearance of wave-like structures in the diffusion region, particularly for the cases where $T_{i0}/T_{e0} = 1/10$ and $1/50$. These structures suggest the presence of underlying kinetic instabilities, likely associated with IAWs. To better understand the origin of this wave activity, we now focus on a detailed analysis of the diffusion region.

To isolate the waveforms specifically associated with the instability, we concentrate on the outflow electric field, E_x. This approach helps to avoid interference from background electromagnetic field structures, as the baseline outflow electric field is much weaker than the observed fluctuations. As a result, any detected E_x perturbations can be directly attributed to wave activity. Figure 5 highlights the regions where large-amplitude waveforms of the outflow electric field are concentrated, indicating that these waves are generated and confined in regions where the outflow electron–ion drift velocity significantly exceeds the IAI threshold drift. These observations, combined with the absence of significant wave activity in the

https://doi.org/10.1017/S002237782510113X Published online by Cambridge University Press

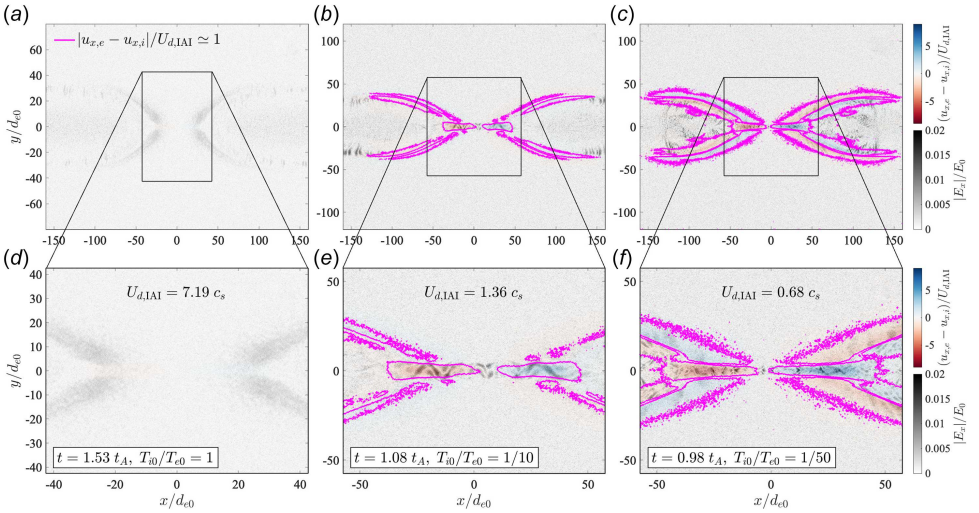

FIGURE 5. Colourmap displaying the x-component of the electron–ion drift velocity normalised to the IAI threshold drifts, calculated with local ion-acoustic speeds $c_s=\sqrt{(T_{e,xx}+3T_{i,xx})/m_i}$ (red-blue), overlaid with contours indicating the regions where $|u_{x,e}-u_{x,i}|/U_{d,\mathrm{IAI}}\simeq 1$ (magenta) and the magnitude of the outflow electric field (E_x, normalised to the reference value $E_0=m_ec\omega_{pe}/e$ and in grey scale) shortly after the time of maximum reconnection rate (see figure 2). This is shown for the following cases: (*a,d*) $T_{i0}/T_{e0}=1$; (*b,e*) $T_{i0}/T_{e0}=1/10$ and (*c,f*) $T_{i0}/T_{e0}=1/50$. Panels (*d*)–(*f*) zoom in on the diffusion region, as identified by the boxes in panels (*a*)–(*c*).

$T_{i0}/T_{e0}=1$ case, strongly suggest that the waveforms are generated by IAI, triggered by the large outflow current.

The evolution of these waveforms for $T_{i0}/T_{e0}=1/50$ is depicted in figure 6(*a,b*), showing the outflow electric field near the x-point along the outflow symmetry line ($y=0$) as a function of x and t. By performing two-dimensional Fourier transforms, we obtain spectra of the outflow electric field near the x-point, shown in figure 6(*c,d*). These spectra are compared with the solutions to the linearised Vlasov–Poisson equation (2.4), first assuming zero ion drift (in the lab frame) to obtain $\omega_{\mathrm{Vlasov}}(k)$ (shown as the blue dashed line) and then Doppler-shifted by the maximum ion outflow drift at the outflow ends of the current sheet (red dashed line; we find that $u_{x,i}$ reaches $u_{x,i,\max}\simeq 0.8v_{A,i0}$ along the outflow symmetry line before IAI saturates and the current sheet becomes strongly nonlinear). The Doppler-shifted solution to the linearised Vlasov–Poisson equations is calculated as simply

$$\omega_{\mathrm{DS}}=\omega_{\mathrm{Vlasov}}\pm ku_{x,i,\max}, \tag{4.1}$$

where the $\pm$ denotes a Doppler shift for positive ion drift (to the right of the x-point, $x>0$) and negative ion drift (to the left of the x-point, $x<0$), respectively.[4]

[4]To demonstrate the bidirectional nature of IAWs, we analysed the spectra from regions either to the left ($x<0$) or to the right ($x>0$) of the x-point (see figures 6*c* and 6*d*, respectively). In this analysis, we observe that modes associated with the solutions to (2.4) and indicative of IAWs display both positive and negative slopes in frequency space, confirming their bidirectional nature. This evidence supports our assertion that IAWs generated near the x-point propagate both towards and away from the x-point.

https://doi.org/10.1017/S002237782510113X Published online by Cambridge University Press

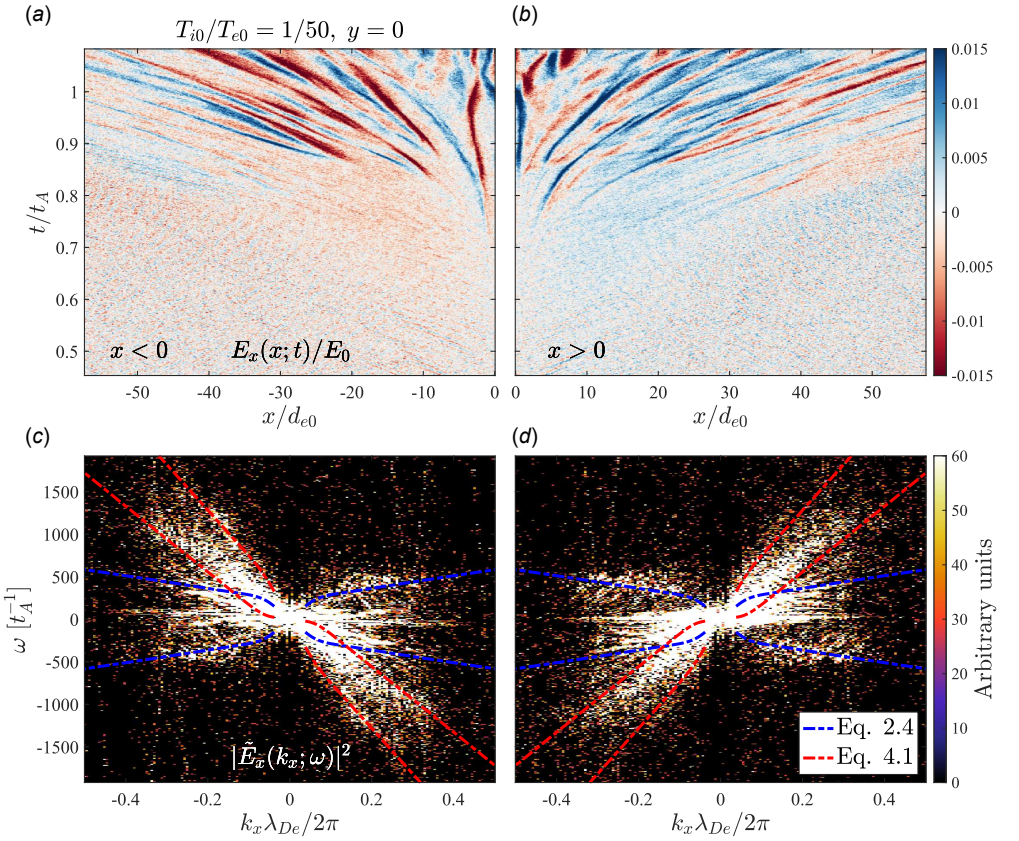

FIGURE 6. (*a,b*) Outflow electric field component (E_x) near the x-point along the outflow symmetry line ($y = 0$) as a function of x and t for $T_{i0}/T_{e0} = 1/50$ and (*c,d*) the squared two-dimensional spectrum $|\tilde{E}(k_x;\omega)|^2$ of the (*a,c*) $x < 0$ and (*b,d*) $x > 0$ halves of the data. The spectrum is overlaid with the parallel wave mode solution to the linearised Vlasov–Poisson equations ((2.4), in blue) for an electron–ion drift speed of $U_d = v_{A,e} - v_{A,i}$, corresponding to an approximation of the maximum drift that can be reached in this system (though we note that $\mathrm{Re}(\omega)$ is largely insensitive to this parameter). Additionally, (4.1) is shown for a positive maximum ion drift (to the right of the x-point, $x > 0$) and negative maximum ion drift (to the left of the x-point, $x < 0$).

While these two solutions clearly bare on the numerical data, we also note that the spectra are far richer than the linear theory discussed previously would predict. One reason for this discrepancy could be that (2.4) and (4.1) ignore both the presence of background magnetic fields as well as electromagnetic effects. Strictly speaking, these limitations imply that our analytical calculations are only expected to be valid along the outflow symmetry line, in the immediate vicinity of the x-point (and apply only to longitudinal modes, i.e. modes such that $\boldsymbol{k} \parallel \boldsymbol{E}$). An unsimplified linear analysis of this problem, fully accounting for the specific geometric configuration of reconnection, is analytically intractable; and so, we are unable to check whether indeed this is the source of discrepancy. However, we think it is more likely that figure 6 displays evidence for nonlinear effects, as discussed later.

Beyond the alignment with the linear Vlasov–Poisson solution, the spectra in figure 6 also show lower frequency modes under the curves corresponding to (2.4).

https://doi.org/10.1017/S002237782510113X Published online by Cambridge University Press

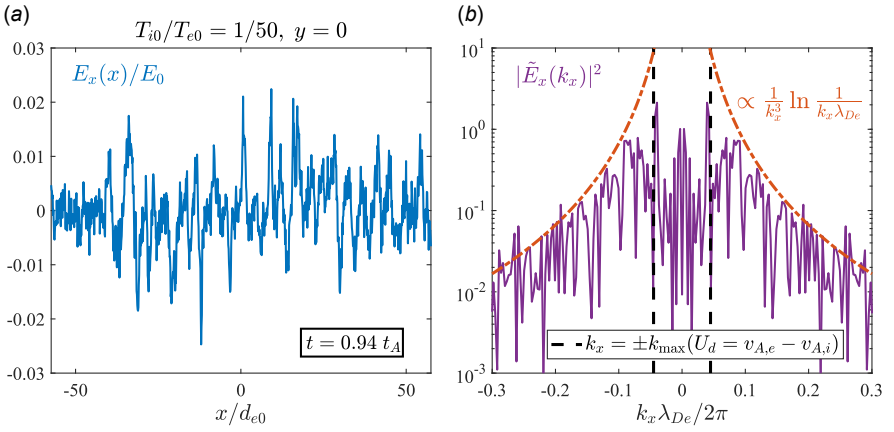

FIGURE 7. (*a*) Outflow electric field and (*b*) the wavenumber spectrum along the outflow symmetry line ($y = 0$) for $T_{i0}/T_{e0} = 1/50$ some time shortly after the peak reconnection rate, compared with the KP spectrum (dash-dotted curve) and the wavenumber of the fastest-growing IAI mode at drift $U_d = v_{A,e} - v_{A,i}$, based on the data in figure 1, indicated by the dashed lines.

These modes emerge more clearly when performing one-dimensional transforms of the outflow electric field near the x-point, as seen in figure 7(*b*). Remarkably, the resulting one-dimensional spectrum $|\tilde{E}_x(k_x)|^2$ along the outflow symmetry line agrees closely with the Kadomtsev–Petviashvili (KP) spectrum (Kadomtsev & Petviashvili 1962; Petviashvili 1963; Liu *et al*. 2024) for values of $k_x\lambda_{De}/2\pi > 0.1$, suggesting that, in our simulations, saturation of IAI occurs through strong nonlinear ion effects (induced scattering) – and indeed, there is clear evidence for ion phase-space holes in figure 4, as also reported by Zhang *et al*. (2023) – and through the quasilinear relaxation of electrons when the electron distribution develops a significant plateau (not shown in this paper, but confirmed via 1-D slices of the electron distribution during the saturation stages of IAI).

Also notable in figure 7 is the remarkable agreement between the peak at low values of k_x with the wavenumber of the fastest-growing IAI mode for values of the drift velocity $U_d = v_{A,e} - v_{A,i}$ (corresponding to an approximation of the maximum drift that can be reached in this system), based on the data in figure 1, identified as the vertical black dashed lines. This suggests that in our simulations, IAWs are first generated at these low-k when IAI is triggered and, through induced scattering off thermal ions, redistribute in k-space, thus populating the KP spectrum.

We conclude from the analysis of this section that the nonlinear wave activity that we observe in the current sheet is most likely induced by IAI. In the following sections, we analyse the effects of this instability on the reconnection process.

4.4. *Effects of IAI on magnetic reconnection*

This section examines the effects of IAI on collisionless magnetic reconnection, focusing first on the ion heating facilitated by IAI and subsequently on the anomalous contributions to the ion and electron momentum equations.

4.4.1. Ion heating

Our simulations reveal substantial ion heating in cold ion runs, particularly in the xx component of the ion temperature tensor, as demonstrated in figures 8 and 9,

https://doi.org/10.1017/S002237782510113X Published online by Cambridge University Press

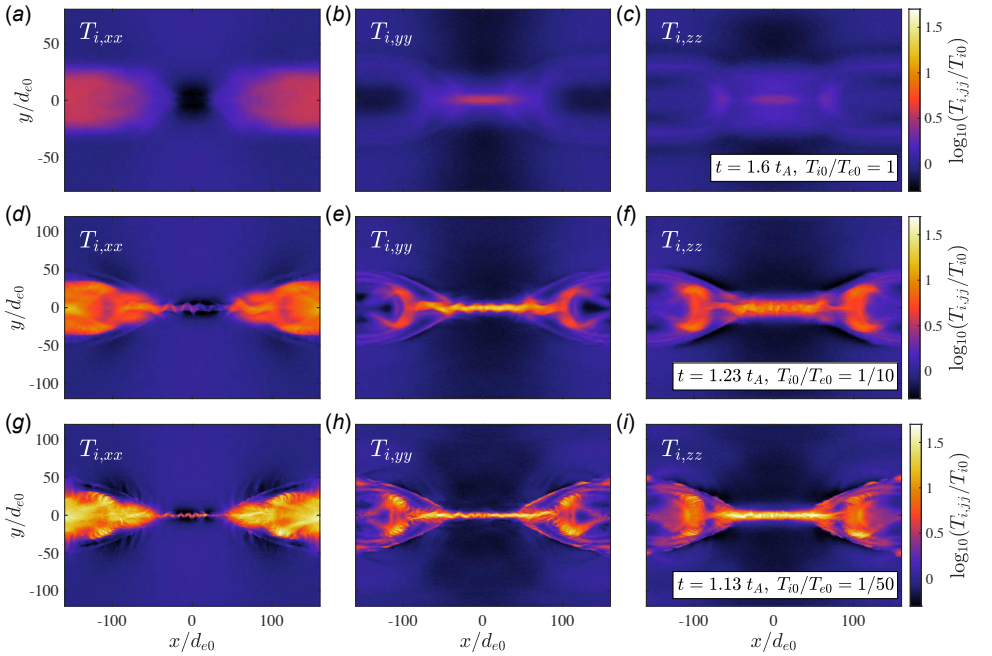

FIGURE 8. Comparison of the logarithm (base 10) of the ion temperature tensor elements (*a,d,g*) T_{xx}, (*b,e,h*) T_{yy} and (*c,f,i*) T_{zz}, normalised to the initial ion temperature T_{i0}, some time after the peak reconnection rate for (*a,b,c*) $T_{i0}/T_{e0} = 1$, (*d,e,f*) $1/10$ and (*g,h,i*) $1/50$.

which show the diagonal elements of the ion temperature tensor, normalised to T_{i0}, over the entire simulation domain, and their evolution along the outflow symmetry line, respectively. Due to reconnection dynamics, $T_{i,xx}$ undergoes an initial cooling to below T_{i0} near the x-point (see Appendix B). Subsequently, when the initial ratio is $T_{i0}/T_{e0} = 1/10$ and $1/50$ (and thus, IAI is strongly triggered), $T_{i,xx}$ rises to $\approx T_e/10$ throughout the current sheet (while the electrons remain essentially unheated, so $T_e \approx T_{e0}$). In contrast, no comparable heating is observed in the equal-temperature run ($T_{i0}/T_{e0} = 1$), where $T_{i,xx}$ remains below T_{i0} at the x-point.

Although we have so far focused on the onset of in-plane IAI and the generation of IAWs in just the outflow direction, we similarly expect IAI to be triggered in the inflow direction, but more weakly so because the inflow electron–ion drift speeds $|U_{d,\mathrm{inflow}}| = |u_{y,e} - u_{y,i}|$ are smaller than $|U_{d,\mathrm{outflow}}|$ by approximately a factor of the reconnection rate $\mathcal{R}$. Furthermore, we already expect some heating in $T_{i,yy}$ during the onset of reconnection (see Appendix B), which elevates the threshold drift speed needed to trigger IAI. Still, we find that there are indeed regions in the vicinity of the current sheet where $|U_{d,\mathrm{inflow}}| > U_{d,\mathrm{IAI}}$ (see Appendix C) which likely explains the added increases to $T_{i,yy}$ after IAI is triggered near the x-point.

Finally, figures 8 and 9 likewise show that $T_{i,zz}$ reaches values comparable to T_e. We do not, however, attribute this heating to IAI, but rather to the reconnection electric field E_z (see Appendix B). During the late stages of IAI, we might expect $T_{i,zz}$ (along with the other diagonal elements of the ion temperature tensor) to additionally pick up small-scale fluctuations, due to the highly non-Maxwellian nature of the velocity distributions at these times (see figure 4), but IAI itself is not the primary mechanism for raising $T_{i,zz}$.

https://doi.org/10.1017/S002237782510113X Published online by Cambridge University Press

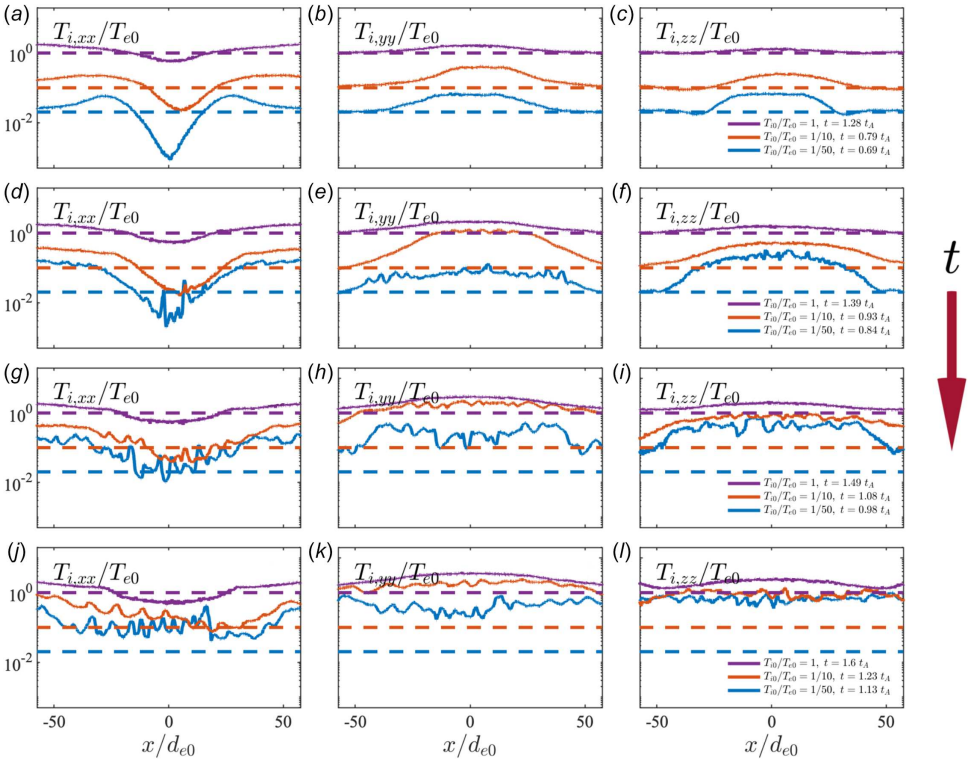

FIGURE 9. Comparison of the ion temperature tensor elements (*a,d,g,j*) T_{xx}, (*b,e,h,k*) T_{yy} and (*c,f,i,l*) T_{zz}, normalised to the initial electron temperature T_{e0}, along the outflow symmetry line ($y = 0$), near the x-point, at times (*a–c*) before and (*d–l*) after the peak reconnection rate for $T_{i0}/T_{e0} = 1$ (in purple), $1/10$ (in orange) and $1/50$ (in blue). The dashed lines in each panel indicate the initial temperature ratio corresponding to its colour.

Our finding that $T_{i,xx}$ drops in the diffusion region while $T_{i,zz}$ rises up to $\sim T_e$ due to reconnection dynamics raises the somewhat surprising possibility that out-of-plane IAI might be less strongly triggered, if at all, than its in-plane counterpart. Fully three-dimensional simulations are however required to validate this speculation.

4.4.2. Anomalous contributions

The presence of small-scale fluctuations in the current sheet allows for a (standard) decomposition of the fields into mean and fluctuating parts, and the computation of so-called anomalous terms in the momentum equations,

$$\boldsymbol{D}_\alpha \equiv -\frac{\langle \delta n_\alpha \delta \boldsymbol{E} \rangle}{\langle n_\alpha \rangle}, \tag{4.2}$$

$$\boldsymbol{T}_\alpha \equiv -\frac{\langle n_\alpha (\boldsymbol{u}_\alpha \times \boldsymbol{B}) \rangle}{\langle n_\alpha \rangle c} + \frac{\langle \boldsymbol{u}_\alpha \rangle \times \langle \boldsymbol{B} \rangle}{c}, \tag{4.3}$$

$$\boldsymbol{I}_\alpha \equiv \frac{m_\alpha}{q_\alpha \langle n_\alpha \rangle} \left[\langle \nabla \cdot (\boldsymbol{u}_\alpha \boldsymbol{u}_\alpha n_\alpha) \rangle - \nabla \cdot (\langle \boldsymbol{u}_\alpha \rangle \langle \boldsymbol{u}_\alpha \rangle \langle n_\alpha \rangle) \right], \tag{4.4}$$

https://doi.org/10.1017/S002237782510113X Published online by Cambridge University Press

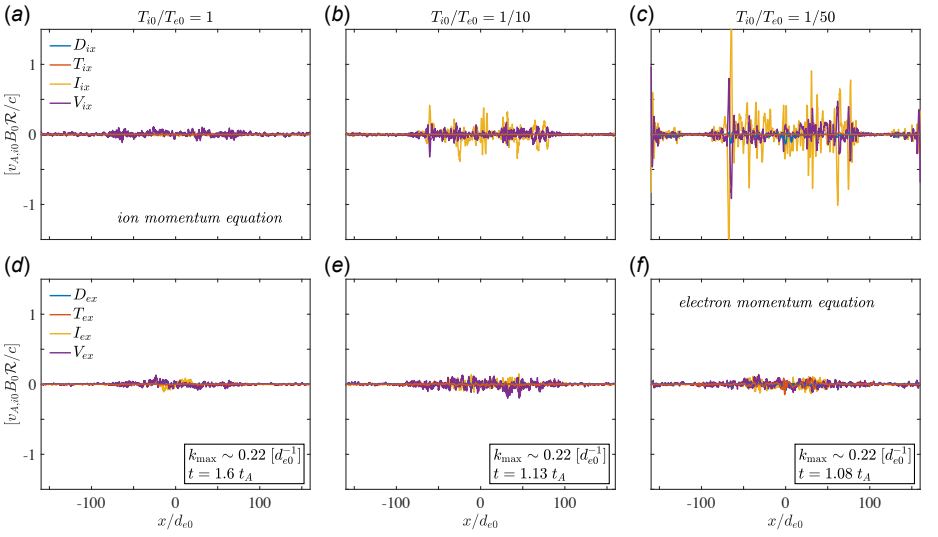

FIGURE 10. Comparison of the anomalous contributions (4.2) to (4.5), normalised to $v_{A,i0}B_0\mathcal{R}/c$ with $\mathcal{R} = 0.2$, obtained from simulations using the (*a,b,c*) ion and (*d,e,f*) electron momentum equations along the outflow symmetry line ($y = 0$) some time after the peak reconnection rate for (*a,d*) $T_{i0}/T_{e0} = 1$, (*b,e*) 1/10 and (*c,f*) 1/50. The maximum allowed k indicated at the lower right corner of panels (*d*)–(*f*) corresponds to the reciprocal of the length of the window size in which the Savitzky–Golay filter is implemented (see Appendix D).

$$\boldsymbol{V}_\alpha \equiv \frac{m_\alpha}{q_\alpha \langle n_\alpha \rangle} \frac{\partial}{\partial t} \langle \delta n_\alpha \delta \boldsymbol{u}_\alpha \rangle, \tag{4.5}$$

by performing two-dimensional spatial averaging in the plane of reconnection (see Appendix D for the derivation of the anomalous terms and a detailed description of the averaging procedure). Here, $\boldsymbol{D}_\alpha$ is the anomalous drag (or resistivity), $\boldsymbol{T}_\alpha$ is the anomalous viscosity (momentum transport), $\boldsymbol{I}_\alpha$ is the anomalous Reynolds stress and $\boldsymbol{V}_\alpha$ is associated with fluctuating flows (Che, Drake & Swisdak 2011; Graham *et al*. 2022).

Figure 10 shows the anomalous contributions obtained from simulations by spatially averaging the momentum equation along the outflow symmetry line some time after the peak reconnection rate. We normalise the anomalous terms to $v_{A,i0}B_0\mathcal{R}/c$, where we have taken the (normalised) reconnection rate $\mathcal{R}$ to be approximately 0.2 (guided by the data in figure 2). As shown in these figures, we find that for systems with low initial ion–electron temperature ratios, anomalous Reynolds stress dominates the anomalous contributions to the ion momentum equation. Although the overall reconnection rate remains largely unaffected by IAI (see figure 2), the localised dynamics in the diffusion region demonstrate significant fluctuations in both the Reynolds stress (as seen in I_{ix} spikes in figure 10) and the anomalous flow term V_{ix}. These spikes suggest the emergence of small-scale shear flows and turbulence driven by IAI-induced density and flow fluctuations, which can potentially explain the fluctuations in the reconnection rate shown in figure 2 after the

https://doi.org/10.1017/S002237782510113X Published online by Cambridge University Press

reconnection rate peaks and IAI is strongly triggered for $T_{i0}/T_{e0} = 1/10$ and $1/50$.[5] In contrast, anomalous contributions to the electron momentum equation are negligible compared with $v_{A,i0}B_0\mathcal{R}/c$. Importantly, when averaged over the diffusion region, all anomalous terms – both to the ion and electron momentum equations – are nearly zero, suggesting that IAI does not significantly affect coherent d_i-scale structures through these anomalous terms.

Previous numerical studies have reported that IAI may produce significant anomalous resistivity (Watt, Horne & Freeman 2002; Petkaki *et al*. 2003, 2006; Hellinger, Trávníček & Menietti 2004). However, these studies often begin with super-critical configurations that can artificially amplify wave energy, potentially explaining the discrepancy between earlier results and our findings, which seem to indicate that although IAI causes substantial ion heating, it does not contribute to large-scale anomalous effects, at least in the context of magnetic reconnection. This diverges from the conclusions of Rudakov & Korablev (1966) and Bychenkov, Silin & Uryupin (1988) because our system never reaches a hypothetical steady-state regime in which ion-acoustic turbulence drags enough momentum from the electrons to reduce the in-plane current. Rudakov & Korablev (1966) and Bychenkov *et al*. (1988) assumed that the electron–ion drift stabilises near the ion-sound speed once the instability saturates, which is only true if just the resonant electrons are taken into account. The bulk of the fast tail, which carries most of the current, remains non-resonant and is freely accelerated due to reconnection dynamics (e.g. magnetic tension forces, electron pressure gradient). Consequently, the anomalous resistivity in our simulations is much lower than the theoretical estimate – a result that aligns with recent analyses of IAI (Liu *et al*. 2024).

5. Conclusions

This study presents comprehensive numerical evidence for the excitation of the ion-acoustic instability (IAI) within the diffusion region of a reconnecting magnetic configuration, underscoring the important role of this kinetic instability in influencing reconnection dynamics in environments where the upstream ion–electron temperature ratio is significantly below unity.

In cases with low ion–electron temperature ratios, our results show that IAI induces significant ion heating, such that the ion temperature along the reconnection outflow rises to $\approx T_e/10$. However, we find that IAI has only a limited impact on the anomalous contributions to the momentum equations and the overall reconnection rate: in contrast to earlier studies reporting substantial anomalous resistivity (under super-critical conditions), our findings indicate that the anomalous effects of IAI on momentum transport are minimal. An implication of this result is that – unlike widely assumed in the literature – IAI cannot be relied upon to provide the anomalous resistivity necessary to enable a Petschek-like opening of the reconnection exhaust (Petschek 1964; Ugai & Tsuda 1977; Scholer & Roth 1987; Biskamp 2000; Erkaev, Semenov & Jamitzky 2000; Uzdensky 2003; Kulsrud 2014). Indeed,

[5]The strong I_{ix} and V_{ix} spikes in figure 10 are shown to be comparable to $v_{A,i0}B_0\mathcal{R}/c$ for cold-ion runs, which is roughly of the order of the $(\boldsymbol{u}_i \times \boldsymbol{B})_x/c = -u_{iz}B_y/c$ term in the ion momentum equation at the outflows and approximately equal to the magnitude of the reconnection electric field. These anomalous contributions may then have an appreciable effect on the bulk ion outflow speed u_{ix}, which presents itself as fluctuations in the reconnection rate (as seen in figure 2). Indeed, these fluctuations occur on time scales compatible with the E_x waveforms seen in figure 6. However, since these anomalous terms are negligible compared with $v_{A,i0}B_0\mathcal{R}/c$ when averaged over the diffusion region, they cannot significantly affect the global behaviour of the reconnection rate.

https://doi.org/10.1017/S002237782510113X Published online by Cambridge University Press

our simulations, while exhibiting high reconnection rates, do not display Petshek-like geometries.

We speculate that the dynamics investigated here would be largely unaffected if a more realistic mass ratio were used. First, as detailed by Liu *et al*. (2024), the mass ratio does not seem to have a strong effect on the final T_i/T_e. Second, according to (4.2), the anomalous resistivity due to ion-acoustic turbulence scales with the amplitude of the turbulent electric field, which itself scales with $(m_i/m_e)^{1/4}$ in quasilinear calculations (e.g. Liu *et al*. 2024). The implementation of a realistic mass ratio would then, at most,[6] result in a factor of $\sim$2 increase in the amplitude of ion-acoustic fluctuations that we see in our simulations, implying that the anomalous resistivity would remain negligible.

We further speculate that these results may have broader implications for ion heating in the solar wind, as it is understood that solar wind turbulence is pervaded by numerous reconnection sites (Retinò *et al*. 2007; Servidio *et al*. 2009, 2011; Osman *et al*. 2014), and the partitioning of energy at these sites could be partially governed by instabilities like IAI. As discussed in § 1, spacecraft observations have consistently reported the existence of solar wind patches with low ion–electron temperature ratios and substantial but poorly understood ion heating across vast distances in the solar wind. One suggested explanation for such heating is that it may be due to IAI-mediated energy conversion in reconnection sites, spontaneously arising via turbulent dynamics. We argue in Appendix E that the standard description of turbulence at sub-ion scales in the solar wind allows for a significant range of scales where indeed one might expect IAI to be triggered.

While our focus in this analysis is primarily on waveform generation near the x-point due to large electron–ion drifts, it is important to note that similar drift-driven wave activity is also observed along and near the separatrix (somewhat visible in figure 5). The electron–ion drifts in these regions are similarly large, leading to the generation of waveforms and the further heating of ions. However, as reported in previous numerical studies, kinetic processes other than IAI likely contribute to the observed wave activity in those regions, such as two-stream or counter-streaming instabilities (Fujimoto 2014; Chen *et al*. 2015; Hesse *et al*. 2018) and the Kelvin–Helmholtz instability (Divin *et al*. 2012; Fermo, Drake & Swisdak 2012; Lapenta *et al*. 2014). These additional instabilities near the separatrix play a complementary role in shaping the broader reconnection environment. Future studies could explore the interaction of these instabilities further to develop a more comprehensive understanding of the complex kinetic processes governing collisionless magnetic reconnection.

Acknowledgments

The authors extend their gratitude to Kyle G. Miller for his valuable insights on PIC simulations and to Muni Zhou for engaging discussions. The authors thank an anonymous referee for suggestions that significantly improved this paper. The

[6]We say 'at most' because estimating the effective electric field that drives the electron drift, $E_{\text{in-plane}}$, as $(\boldsymbol{u}_e \times \boldsymbol{B})_x/c$ implies that it is of the order of $E_{NL} = m_e c_{s0}\omega_{pi} T_{e0}/(6\pi e T_{i0})$, the characteristic nonlinear electric field that separates the quasilinear and nonlinear regimes of ion-acoustic turbulence (e.g. Bychenkov et al. 1988; Liu et al. 2024). This may then give rise to larger values of anomalous resistivity than expected in a situation where quasilinear theory applies, i.e. $E_{\text{in-plane}}/E_{NL} \ll 1$. In simulations with realistic mass ratio and separation between the speed of light and the electron Alfvén speed, we expect this inequality to hold and, therefore, even lower values of the anomalous resistivity than we measure in our simulations.

https://doi.org/10.1017/S002237782510113X Published online by Cambridge University Press

authors also acknowledge the OSIRIS Consortium, comprising UCLA and Instituto Superior Técnico (IST) in Lisbon, Portugal, for providing access to the OSIRIS 4.0 framework.

Editor Dmitri Uzdensky thanks the referees for their advice in evaluating this article.

Funding

This research was partially funded by DOE awards DE-SC0022012 and DE-FG02-91ER54109. Additionally, this research utilized resources of the MIT-PSFC partition of the Engaging cluster at the MGHPCC facility, funded by DOE award No. DE-FG02-91ER54109 and the National Energy Research Scientific Computing Center, a DOE Office of Science User Facility, supported by the U.S. Department of Energy under Contract No. DE-AC02-05CH11231 using NERSC award FES-ERCAP0026577. This material is based upon work supported by the National Science Foundation Graduate Research Fellowship Program under Grant No. 2141064. Any opinions, findings, and conclusions or recommendations expressed in this material are those of the author(s) and do not necessarily reflect the views of the National Science Foundation.

Declaration of interests

The authors report no conflict of interest.

Data availability statement

The data that support the findings of this study are available from the corresponding author upon reasonable request.

Appendix A. Temperature dependence of the IAI wavenumber associated with a marginally stable system

In figure 1, we illustrate that the wavenumber associated with a marginally stable system ($\gamma_{\max} = 0$) increases sharply as T_{i0}/T_{e0} decreases below approximately $1/10$. This behaviour arises in the regime where $U_d \ll v_{\mathrm{th},e}$ and $T_i \ll T_e$. In that limit, $c_s = \sqrt{(\gamma_e T_e + \gamma_i T_i)/m_i} \simeq \sqrt{T_e/m_i} \gg v_{\mathrm{th},i}$ ($\gamma_e = 1$ for isothermal electrons). Thus, at the ion-acoustic resonance ($\omega \simeq k c_s$), one obtains

$$|\zeta_i| \equiv |\omega/(\sqrt{2} k v_{\mathrm{th},i})| \gg 1 \tag{A1}$$

and

$$|\zeta_e| \equiv |(\omega - \boldsymbol{k}\cdot\boldsymbol{U}_d)/(\sqrt{2} k v_{\mathrm{th},e})| \ll 1. \tag{A2}$$

Substituting these conditions into (2.4) then leads to (Fitzpatrick 2016)

$$2(k\lambda_{De})^2 \simeq \frac{T_e}{T_i}\frac{1}{\zeta_i^2} - 2 - 2i\sqrt{\pi}\left(\frac{T_e}{T_i}\zeta_i e^{-\zeta_i^2} + \zeta_e\right) \tag{A3}$$

and approximately (Biskamp 2000)

$$[\mathrm{Re}(\omega)]^2 \simeq \frac{k^2 c_s^2}{1 + k^2\lambda_{De}^2}, \tag{A4}$$

assuming that $\gamma \equiv \mathrm{Im}(\omega) \ll \mathrm{Re}(\omega)$.

https://doi.org/10.1017/S002237782510113X Published online by Cambridge University Press

It has been shown (Fried & Gould 1961) that the critical drift velocity for IAI is approximately $U_{d,\mathrm{IAI}} \simeq 4\sqrt{2}v_{\mathrm{th},i}$ when $T_i/T_e < 1/20$, and is of order c_s for higher temperature ratios (e.g. $1/20 \lesssim T_i/T_e \lesssim 1$). Combining this with (A3) (upon ignoring the exponential term) and (A4) yields the final result

$$k^2(\gamma_{\max}=0)\lambda_{De}^2 \simeq \begin{cases} (32T_i/T_e)^{-1}-1, & T_i/T_e \lesssim 1/20, \\ 0, & 1/20 \lesssim T_i/T_e \lesssim 1. \end{cases} \tag{A5}$$

For $T_i/T_e = 1/50$, (A5) gives $k \approx 0.12\,[2\pi/\lambda_{De}]$, which is in close agreement with the solution presented in figure 1 ($k_{\max}(\gamma_{\max}=0) \approx 0.09\,[2\pi/\lambda_{De}]$). Equation (A5) makes it evident that $k(\gamma_{\max}=0)$ increases with decreasing T_i/T_e and also clarifies why $k_{\max}$ at $\gamma_{\max}=0$ becomes (or remains) zero when T_i/T_e increases beyond $1/10$ (see figure 1). It is interesting to note that (A5) does not involve the ion–electron mass ratio, implying that when IAI just begins to become unstable, the same behaviour of $k_{\max}$ would emerge even if a more realistic ratio (e.g. $m_i/m_e = 1836$) were used.

Appendix B. Diagonal ion temperature tensor elements at the x-point in the absence of IAI

Taking the second moment of the Vlasov equation yields the evolution of the pressure tensor (e.g. Ng et al. 2020*b*)

$$\frac{\partial \mathcal{P}_{lm}}{\partial t} + \frac{\partial \mathcal{Q}_{lmn}}{\partial x_n} = nqu_{[l}E_{m]} + \frac{q}{m}\epsilon_{[lnp}\mathcal{P}_{nm]}\frac{B_p}{c}, \tag{B1}$$

where the square brackets denote a sum over permutations of the indices (e.g. $u_{[l}E_{m]} = u_lE_m + u_mE_l$), $\mathcal{P}_{lm}$ and $\mathcal{Q}_{lmn}$ are the second and third moments of the distribution function,

$$\mathcal{P}_{lm} = m\int \mathrm{d}^3v\; v_lv_mf = P_{lm} + mnu_lu_m, \tag{B2a}$$

$$\mathcal{Q}_{lmn} = m\int \mathrm{d}^3v\; v_lv_mv_nf = q_{lmn} + u_{[l}\mathcal{P}_{mn]} - 2mnu_lu_mu_n, \tag{B2b}$$

and q_{lmn} is the heat flux tensor.

The ion momentum equation is

$$\boldsymbol{E}' = \frac{m_i}{en_i}\left[\frac{\partial}{\partial t}(n_i\boldsymbol{u}_i) + \boldsymbol{\nabla}\cdot(\boldsymbol{u}_i\boldsymbol{u}_in_i)\right] + \frac{1}{en_i}\boldsymbol{\nabla}\cdot\boldsymbol{P}_i, \tag{B3}$$

where $\boldsymbol{E}' = \boldsymbol{E} + \boldsymbol{u}_i\times\boldsymbol{B}/c$ is the non-ideal electric field, $\boldsymbol{P}_i$ is the ion pressure tensor and the resistivity is neglected for collisionless reconnection.

At the x-point, due to symmetry, it is approximately true that

$$\partial_y u_{ix}\big|_X = \partial_x u_{iy}\big|_X = u_{ix,X} = u_{iy,X} = 0, \tag{B4a}$$

$$\boldsymbol{\nabla}u_{iz}|_X = \boldsymbol{B}_X = \boldsymbol{0}. \tag{B4b}$$

Assuming steady-state ($\partial_t = 0$) and uniform density near the x-point, the xx, yy and zz components of (B1), the z component of (B3), and (B4*a*) and (B4*b*) give

$$\partial_x q_{i,xxx}\big|_X + \partial_y q_{i,xxy}\big|_X + n_{i,X}T_{i,xx,X}\left(3\partial_x u_{ix}\big|_X + \partial_y u_{iy}\big|_X\right) = 0, \tag{B5a}$$

https://doi.org/10.1017/S002237782510113X Published online by Cambridge University Press

$$\partial_x q_{i,yyx}\big|_X + \partial_y q_{i,yyy}\big|_X + n_{i,X} T_{i,yy,X}\left(\partial_x u_{ix}\big|_X + 3\partial_y u_{iy}\big|_X\right) = 0, \tag{B5b}$$

$$\begin{aligned}\partial_x q_{i,zzx}\big|_X + \partial_y q_{i,zzy}\big|_X + n_{i,X}\left[\left(T_{i,zz,X} + m_i u_{iz,X}^2\right)\left(\partial_x u_{ix}\big|_X + \partial_y u_{iy}\big|_X\right)\right] \\ + 2u_{iz,X}\left(\partial_x T_{i,xz}\big|_X + \partial_y T_{i,yz}\big|_X\right) = 2en_{i,X} E_{z,X} u_{iz,X},\end{aligned} \tag{B5c}$$

$$eE_{z,X} = \partial_x T_{i,xz}\big|_X + \partial_y T_{i,yz}\big|_X + m_i u_{iz,X}\left(\partial_x u_{ix}\big|_X + \partial_y u_{iy}\big|_X\right), \tag{B5d}$$

which may be rearranged to read

$$T_{i,xx,X} = -\frac{1}{n_{i,X}} \frac{\partial_x q_{i,xxx}\big|_X + \partial_y q_{i,xxy}\big|_X}{3\partial_x u_{ix}\big|_X + \partial_y u_{iy}\big|_X}, \tag{B6a}$$

$$T_{i,yy,X} = -\frac{1}{n_{i,X}} \frac{\partial_x q_{i,yyx}\big|_X + \partial_y q_{i,yyy}\big|_X}{\partial_x u_{ix}\big|_X + 3\partial_y u_{iy}\big|_X}, \tag{B6b}$$

$$T_{i,zz,X} = m_i u_{iz,X}^2 - \frac{1}{n_{i,X}} \frac{\partial_x q_{i,zzx}\big|_X + \partial_y q_{i,zzy}\big|_X}{\partial_x u_{ix}\big|_X + \partial_y u_{iy}\big|_X}. \tag{B6c}$$

We note that at the x-point, ions experience the reconnection electric field

$$E'_{z,X} = E_{z,X} \approx -\frac{v_{A,i} B_0 \mathcal{R}}{c} \tag{B7}$$

for a duration $\Delta t \sim \delta / v_{\rm in}$, where $\delta \sim d_i \sim d_{i0}$ is the thickness of the ion diffusion region, $v_{\rm in} \sim \mathcal{R} v_{A,i}$ is the inflow speed and $\mathcal{R}$ is the reconnection rate. We may therefore estimate that at the x-point, the out-of-plane ion velocity increases by

$$u_{iz,X} - u_{iz0} \sim \frac{e}{m_i} E'_{z,X} \Delta t \sim -v_{A,i}, \tag{B8}$$

where in our simulations, u_{iz0} is specified by the choices $\omega_{pe}/\Omega_{ce} = 2$ and $\lambda_{\rm B}/d_{i0} = 1$, and the force-balance and Vlasov equilibrium conditions (see § 3). It is written as

$$u_{iz0} = -\frac{c}{2}\sqrt{\frac{m_e}{m_i}}\left(\frac{T_{e0}}{T_{i0}} + 1\right)^{-1}. \tag{B9}$$

Using (B6*a*) to (B6*c*), (B8) and (B9), and considering a zero heat flux leads to

$$T_{i,xx,X} = T_{i,yy,X} = 0, \tag{B10a}$$

$$T_{i,zz,X} \sim \frac{2(T_{e0} + 2T_{i0})^2}{T_{e0} + T_{i0}}, \tag{B10b}$$

where, in writing the right-hand relation of (B10*b*), we have assumed a plasma β of order unity ($8\pi n(T_{i0} + T_{e0}) \sim B_0^2$). It is evident in (B10*b*) that for $T_{i0}/T_{e0} \ll 1$, $T_{i,zz,\max} \sim 2T_{e0} \sim T_{e0}$, which explains that the out-of-plane heating we observe in figures 8 and 9 is due primarily to the reconnection electric field E_z and implies that we expect $T_{i,zz}$ to reach $\sim T_e$ even in the absence of IAI.

https://doi.org/10.1017/S002237782510113X Published online by Cambridge University Press

The fact that (B1), (B4*a*) and (B4*b*) formally lead to the solution (B10*a*) must be recognised as a failure of the fluid model (that is, of the zero heat-flux closure assumed in the derivation). Still, (B10*a*) suggests that $T_{i,xx}$ must undergo a substantial drop from T_{i0} at the x-point – consistent with our simulations (see figures 8 and 9).

However, the zero heat flux assumption also implies a drop in $T_{i,yy}$ below T_{i0} at the x-point, which sharply contradicts our simulation results showing appreciable $T_{i,yy,X}/T_{i0}$, even in runs where IAI does not occur. One reason for this discrepancy could be that such a closure might be more appropriate for $T_{i,xx}$ than for $T_{i,yy}$ because unlike $T_{i,xx}$, ions entering the current sheet gain significant $T_{i,yy}$ in regions of large inflow velocity u_{iy} and could maintain that $T_{i,yy}$ upon arrival at the x-point. We can estimate this local $T_{i,yy}$ increase by examining the approximate yy temperature at the vertical edges of the current sheet (i.e. in the upstream direction), which might be of the same order of magnitude as $T_{i,yy,X}$. Along the inflow symmetry line, $x = 0$, symmetry arguments similar to (B4*a*) and (B4*b*) can be made

$$\begin{aligned}\partial_y u_{ix}\big|_{x=0} &= \partial_x u_{iy}\big|_{x=0} = \partial_x u_{iz}\big|_{x=0} \\ &= u_{ix}(x=0) = B_y(x=0) = B_z(x=0) = 0,\end{aligned} \tag{B11}$$

which applied to the yy and zz components of (B1) and (B3) yields the relations

$$\begin{aligned}u_{iy}[-2eE_y + 2\partial_x T_{i,xy} + 3\partial_y T_{i,yy} + m_i u_{iy}(\partial_x u_{ix} + 3\partial_y u_{iy})] \\ = 2\Omega_{ix}(T_{i,yz} + m_i u_{iy} u_{iz}) - T_{i,yy}(\partial_x u_{ix} + 3\partial_y u_{iy}),\end{aligned} \tag{B12a}$$

$$\begin{aligned}u_{iz}[-2eE_z + 2\partial_x T_{i,xz} + 2\partial_y T_{i,yz} + 2m_i u_{iy}\partial_y u_{iz} + m_i u_{iz}(\partial_x u_{ix} + \partial_y u_{iy})] \\ = -2\Omega_{ix}(T_{i,yz} + m_i u_{iy} u_{iz}) - u_{iy}\partial_y T_{i,zz} \\ -2T_{i,yz}\partial_y u_{iz} - T_{i,zz}(\partial_x u_{ix} + \partial_y u_{iy}),\end{aligned} \tag{B12b}$$

$$\partial_x T_{i,xy} + \partial_y T_{i,yy} + m_i u_{iy}(\partial_x u_{ix} + 2\partial_y u_{iy}) = eE_y + m_i \Omega_{ix} u_{iz}, \tag{B12c}$$

$$\begin{aligned}\partial_x T_{i,xz} + \partial_y T_{i,yz} + m_i u_{iy}\partial_y u_{iz} + m_i u_{iz}(\partial_x u_{ix} + \partial_y u_{iy}) \\ = eE_z - m_i \Omega_{ix} u_{iy},\end{aligned} \tag{B12d}$$

where $\Omega_{ix} \equiv eB_x/(m_i c)$ and we have made the simplifying assumption that heat flux away from the x-point (but not at the x-point) is negligible, i.e. $\partial_n q_{lmn} = 0$.

Since we are considering steady-state and uniform density, the continuity equation gives the incompressibility condition

$$\nabla \cdot \boldsymbol{u}_i = 0, \tag{B13}$$

which combined with (B12*a*)–(B12*d*) gives

$$(-2u_{iy}^{-1}\partial_y u_{iy} - \partial_y)T_{i,yy} = (1 + \Omega_{ix}^{-1}\partial_y u_{iz})^{-1}\partial_y T_{i,zz}, \tag{B14}$$

along $x = 0$ and away from the x-point. We assume that

$$(u_{iz,X} - u_{iz,\delta})^{-1}\partial_y u_{iz}\big|_\delta \approx -u_{iy,\delta}^{-1}\partial_y u_{iy}\big|_\delta \approx d_{i0}^{-1} \gtrsim -T_{i,yy,\delta}^{-1}\partial_y T_{i,yy}\big|_\delta > 0, \tag{B15}$$

where quantities with δ in the subscript indicates values at $x = 0$ and the y-ends of the current sheet, and, in writing the second to last inequality, we have noted that $T_{i,yy}$ might not undergo as drastic of a change from the inflow edges of the current

https://doi.org/10.1017/S002237782510113X Published online by Cambridge University Press

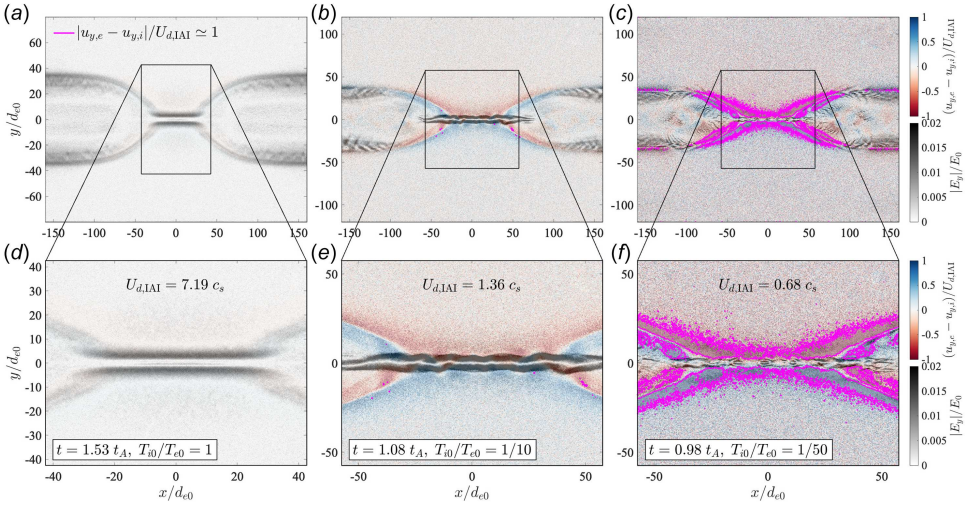

FIGURE 11. Colourmap displaying the y-component of the electron–ion drift velocity normalised to the IAI threshold drifts, calculated with local ion-acoustic speeds $c_s = \sqrt{(T_{e,yy} + 3T_{i,yy})/m_i}$ (red-blue), overlaid with contours indicating the regions where $|u_{y,e} - u_{y,i}|/U_{d,\mathrm{IAI}} \simeq 1$ (magenta) and the magnitude of the inflow electric field (E_y, normalised to the reference value $E_0 = m_e c\omega_{pe}/e$ and in grey scale), plotted at the same times as in figure 5. This is shown for (*a,d*) $T_{i0}/T_{e0} = 1$, (*b,e*) $T_{i0}/T_{e0} = 1/10$ and (*c,f*) $T_{i0}/T_{e0} = 1/50$. Panels (*d*)–(*f*) zoom in on the diffusion region, as identified by the boxes in panels (*a*)–(*c*).

sheet to the x-point compared with, e.g. u_{iy} or u_{iz} since $T_{i,yy,X}$ is not necessarily zero with the inclusion of non-zero heat flux. As mentioned above, we may approximately say

$$T_{i,yy,X} \sim T_{i,yy,\delta}. \tag{B16}$$

From (B6*c*), we have

$$\partial_y T_{i,zz}\big|_\delta \sim 2m_i u_{iz,\delta}\partial_y u_{iz}\big|_\delta, \tag{B17}$$

which combined with (B14) and (B15), and the assumptions that $B_{x,\delta} \approx B_0$ and $u_{iz,\delta} \approx u_{iz0}$, gives

$$4/3 \lesssim T_{i,yy,\delta}/T_{e0} \lesssim 2, \tag{B18}$$

implying that we also expect substantial heating in $T_{i,yy}$ up to $\sim T_e$ in the vicinity of the x-point and in the absence of IAI. IAI triggered in the y-direction near the x-point might be responsible for additional increases in $T_{i,yy}$ after reconnection onset (see Appendix C).

Appendix C. Inflow-driven IAI

Figure 11 illustrates the inflow electron–ion drift velocity and regions where this drift exceeds the IAI threshold drift, calculated with local ion-acoustic speeds $c_s = \sqrt{(T_{e,yy} + 3T_{i,yy})/m_i}$, now with $T_{\alpha,yy}$ instead of $T_{\alpha,xx}$. Also shown is the magnitude of the inflow electric field (E_y) whose perturbations could be associated with inflow IAWs (although the overall structure of the electric field would mostly be influenced by perturbations due to the outflow IAI).

https://doi.org/10.1017/S002237782510113X Published online by Cambridge University Press

We mentioned in § 4.4.1 that we expect the inflow IAI to be less strongly triggered than its outflow counterpart because inflow electron–ion drift speeds are smaller than outflow drift speeds (roughly by a factor of the reconnection rate $\mathcal{R}$) and that the early heating in $T_{i,yy}$ (see Appendix B) raises the threshold to trigger IAI. Indeed, figure 11 shows that $|U_{d,\mathrm{inflow}}|$ is only of the order of the IAI threshold drift and in just the $T_{i0}/T_{e0} = 1/50$ run, whereas there are extensive regions along the outflow where $|U_{d,\mathrm{outflow}}|$ significantly exceeds the threshold for both $T_{i0}/T_{e0} = 1/10$ and 1/50. Nevertheless, the existence of regions where $|U_{d,\mathrm{inflow}}| > U_{d,\mathrm{IAI}}$ may imply that IAI plays a part in heating $T_{i,yy}$ for cases with cold ions. Based on the data in figure 1, the typical wavenumber of the most unstable IAI mode for all ion–electron temperature ratios considered is $\sim 0.05\,[2\pi/\lambda_{De}] \approx 1\,d_{e0}^{-1}$. We find that regardless of T_{i0}/T_{e0}, the full-width at half-maximum (FWHM) of the current sheet reaches a minimum of $\approx 5d_{e0}$ around the times of peak reconnection rate. This is sufficient to accommodate at least one IAW wavelength within the current sheet,[7] and it may then be reasonable to expect that IAI in the y-direction plays some complementary role in shaping the dynamics in the current sheet for the coldest ion run.

Appendix D. Derivation of anomalous terms and numerical averaging procedure

We start from the momentum equation for species α,

$$m_\alpha \frac{\partial}{\partial t}(n_\alpha \boldsymbol{u}_\alpha) + m_\alpha \boldsymbol{\nabla}\cdot(\boldsymbol{u}_\alpha \boldsymbol{u}_\alpha n_\alpha) = q_\alpha n_\alpha \left(\boldsymbol{E} + \frac{\boldsymbol{u}_\alpha \times \boldsymbol{B}}{c}\right) - \boldsymbol{\nabla}\cdot \boldsymbol{P}_\alpha, \tag{D1}$$

where $\boldsymbol{P}_\alpha$ is the pressure tensor and we have neglected collisions. Let us formally decompose each field into quasi-stationary (mean, averaged) and fluctuating components, such that $\mathcal{Q} = \langle \mathcal{Q}\rangle + \delta\mathcal{Q}$. We then find

$$\begin{aligned}\frac{m_\alpha}{q_\alpha \langle n_\alpha\rangle}\left[\frac{\partial}{\partial t}(\langle n_\alpha\rangle\langle \boldsymbol{u}_\alpha\rangle) + \boldsymbol{\nabla}\cdot(\langle \boldsymbol{u}_\alpha\rangle\langle \boldsymbol{u}_\alpha\rangle\langle n_\alpha\rangle)\right] + \boldsymbol{V}_\alpha + \boldsymbol{I}_\alpha \\ = \langle \boldsymbol{E}\rangle - \boldsymbol{D}_\alpha + \frac{\langle \boldsymbol{u}_\alpha\rangle \times \langle \boldsymbol{B}\rangle}{c} - \boldsymbol{T}_\alpha - \frac{\langle \boldsymbol{\nabla}\cdot \boldsymbol{P}_\alpha\rangle}{q_\alpha \langle n_\alpha\rangle},\end{aligned} \tag{D2}$$

where $\boldsymbol{D}_\alpha$, $\boldsymbol{T}_\alpha$, $\boldsymbol{I}_\alpha$ and $\boldsymbol{V}_\alpha$ are defined in (4.2)–(4.5).

Expressions (4.2)–(4.5) are plotted in figure 10 for all T_{i0}/T_{e0} considered at times after the reconnection rate peaks. For obtaining the numerical values in figure 10, $\langle \mathcal{Q}\rangle$ was set as a two-dimensional spatial average in the plane of reconnection, performed using a Savitzky–Golay filter, which improves data precision while maintaining overall signal trends (Savitzky & Golay 1964). The selection of $k_{\max}$ (reciprocal of the length of the filtering window size) was carefully chosen to low-pass filter wavenumbers associated with the fastest-growing IAI modes and to reduce numerical noise. The upper bound of $k_{\max}$ was established based on the noise in the $T_{i0}/T_{e0} = 1$ simulation. Despite this filtering, some residual noise remains visible (see the $T_{i0}/T_{e0} = 1$ plots in figure 10), so it was necessary to select the smallest possible value for $k_{\max}$ that would appropriately reduce this noise. Guided by the data in figure 1, which indicate that the wavenumbers of the fastest-growing IAI modes across all temperature ratios are $\sim 0.05\,[2\pi/\lambda_{De}] \approx 1\,[d_{e0}^{-1}]$, we selected a $k_{\max}$ smaller than this approximate wavenumber to ensure that all contributions from IAWs were filtered out.

[7] In fact, as shown in figure 1, for $T_{i0}/T_{e0} = 1/50$, $k_{\max}$ increases as U_d decreases to $\simeq c_s$.

https://doi.org/10.1017/S002237782510113X Published online by Cambridge University Press

Furthermore, our analysis shows that the initial ion–electron temperature ratio does not significantly affect the width of the current sheet. Across all simulations, the current sheet width (FWHM) at the time of peak reconnection rate remained consistent at $\sim 5d_{e0}$ or $0.5d_{i0}$, allowing for the application of the same filtering technique for all temperature ratios with window sizes corresponding to $k_{\max}^{-1}$.

Appendix E. Possible connection to solar wind heating

To connect our results with conditions in the solar wind, we adopt a standard model of kinetic-Alfvén-wave (KAW) turbulence (Boldyrev & Perez 2012; Zhou, Liu & Loureiro 2023; Liu et al. 2025) to estimate how large the in-plane drift velocity due to turbulent reconnection events at sub-ion scales might become. We consider the range of scales $d_e \ll k_\perp^{-1} \ll \rho_i$, with $\rho_i = v_{\mathrm{th},i}/\Omega_{ci}$ the ion Larmor radius, and invoke the usual scale-by-scale equipartition between density and magnetic perturbations. At transverse scale $\lambda \sim k_\perp^{-1}$, the electrostatic potential obeys $\varphi_\lambda \sim \sqrt{T_{i0}/T_{e0}}(\rho_i v_{A,i}/c)\delta B_{\perp\lambda}$ (Liu et al. 2025), where $\delta B_{\perp\lambda}$ is the field-perpendicular (fluctuating) magnetic field. Including Boldyrev-type intermittency (Boldyrev & Perez 2012), the energy cascade rate (or eddy-turnover rate) for perpendicular fluctuations subject to nonlinear interactions is $\gamma_{nl} \sim 8\pi\varepsilon/(\delta B_{\perp\lambda}^2 p_\lambda)$, where ε denotes the (constant) energy flux, $p_\lambda = (\lambda/\lambda_0)^{3-D} = \lambda/\lambda_0$ (Frisch 1995) is the volume-filling fraction of the two-dimensional structures lying in planes perpendicular to the background magnetic field and the characteristic size λ_0 represents the largest scale of these highly intermittent, quasi-2-D, field-perpendicular structures.

The in-plane IAI due to reconnection between two turbulent eddies becomes unstable when

$$\frac{U_{d,\text{in-plane},\lambda}}{c_s} \sim \frac{v_{A,e,\perp\lambda}}{c_s} \sim \frac{\delta B_{\perp\lambda}}{\sqrt{4\pi n_0 m_e}}\sqrt{\frac{m_i}{T_{e0}}} \gtrsim 1. \tag{E1}$$

Combining $\gamma_{nl} \sim (c/B_0)\varphi_\lambda/\lambda^2$ with the above expressions, we obtain the range of scales where this can occur,

$$\frac{\lambda}{d_i} \gtrsim \frac{1}{\sqrt{8}}\frac{m_e^{3/2}}{m_i^2}\frac{n_0\beta_e^{1/2}}{\varepsilon\lambda_0}T_{e0}^{1/2}T_{i0}, \tag{E2}$$

where $\beta_e \equiv 8\pi n_0 T_{e0}/B_0^2$ is the electron plasma beta and B_0 denotes the constant background (guide) magnetic field strength. The condition for the in-plane IAI to be triggered at any scale ($d_e < \lambda < d_i$) then becomes

$$T_{e0}^{1/2}T_{i0} \lesssim \frac{m_i^{3/2}}{m_e}\frac{\sqrt{8}\varepsilon\lambda_0}{n_0\beta_e^{1/2}}. \tag{E3}$$

Observations of the solar wind by the Ulysses spacecraft (Balogh et al. 1995; Smith, Marsden & Page 1995) suggest that the flux rate is $\varepsilon/(n_0 m_i) \sim 10^2\ \mathrm{J\,kg^{-1}s^{-1}}$ (Sorriso-Valvo et al. 2007), which, combined with established estimates of the solar wind electron plasma beta of $\beta_e \approx 1$ (Wilson III et al. 2018; Halekas et al. 2020) and approximating λ_0 as the outer (energy-injection) perpendicular scale of solar-wind turbulence of $\lambda_C^\perp \sim 10^6$ km (Weygand et al. 2009, 2011), results in the condition (E3) becoming $(T_{i0}^2 T_{e0})^{1/3} \lesssim 10^2$ eV, well above typical solar-wind temperatures (Richardson & Smith 2003; Hellinger et al. 2013; Štverák et al. 2015; Chen 2016; Verscharen et al. 2019; Píša et al. 2021).

https://doi.org/10.1017/S002237782510113X Published online by Cambridge University Press

Essential to the validity of the previous calculation is to check if the reconnection rate is higher than the eddy turnover rate, or there would be no time for two eddies to reconnect before being sheared apart by the turbulence. Assuming that, at these scales, reconnection proceeds as described by the electron-only reconnection model of Liu *et al*. (2025), the reconnection time is $\tau_{\mathrm{rec},\lambda} \sim \sqrt{2}\,(T_{e0}/T_{i0} + 1)^{-1/2}(\lambda/\rho_i)(\lambda/v_{A,i,\perp\lambda})$ and, therefore,

$$\gamma_{nl}\tau_{\mathrm{rec},\lambda} \sim \frac{\sqrt{2}T_{i0}/T_{e0}}{\sqrt{1+T_{i0}/T_{e0}}}, \tag{E4}$$

which is small when the ion–electron temperature ratio T_{i0}/T_{e0} is low, precisely the regime already required for the instability.

An analogous estimate for the out-of-plane drift,

$$\frac{U_{d,\text{out-of-plane},\lambda}}{c_s} \sim \frac{\delta J_\lambda/en_0}{c_s} \sim \frac{c}{4\pi}\frac{\delta B_{\perp\lambda}}{en_0 d_e}\sqrt{\frac{m_i}{T_{e0}}} \gtrsim 1, \tag{E5}$$

recovers exactly the same scale constraint, (E2), and global threshold, (E3). Hence, under solar-wind parameters, both in-plane and out-of-plane IAIs should be readily triggered once thin current sheets reconnect, although, as mentioned in § 4.4.1, we might expect the out-of-plane IAI to be less strongly triggered that its in-plane counterpart.

It is worth noting that the previous derivation assumes $|\delta B_\perp/B_0| \ll 1$, whereas our study focuses on a configuration without a guide field. Although the impact of a finite guide field on in-plane (perpendicular) and out-of-plane (parallel) IAI remains unclear, preliminary simulations including a guide field on the order of the in-plane, far-asymptotic field continue to show similar wave activity in the diffusion region. Future work could investigate in detail how a guide field influences in-plane IAI in the context of reconnection and would be necessary to solidify the validity of the estimates made in this appendix.

REFERENCES

ALT, A. & KUNZ, M.W. 2019 Onset of magnetic reconnection in a collisionless, high-β plasma. *J. Plasma Phys.* **85**, 175850102.

BALOGH, A., SOUTHWOOD, D.J., FORSYTH, R.J., HORBURY, T.S., SMITH, E.J. & TSURUTANI, B.T. 1995 The heliospheric magnetic field over the south polar region of the sun. *Science* **268**, 1007–1010.

BIRN, J. *et al.* 2001 Geospace environmental modeling (GEM) magnetic reconnection challenge. *J. Geophys. Res.: Space Phys.* **106**, 3715–3719.

BISKAMP, D. 2000 *Magnetic Reconnection in Plasmas*. Cambridge University Press.

BOLDYREV, S. & PEREZ, J.C. 2012 Spectrum of kinetic-Alfvén turbulence. *Astrophys. J.* **758**, L44.

BRIDGE, H.S., BELCHER, J.W., BUTLER, R.J., LAZARUS, A.J., MAVRETIC, A.M., SULLIVAN, J.D., SISCOE, G.L. & VASYLIUNAS, V.M. 1977 The plasma experiment on the 1977 voyager mission. *Space Sci. Rev.* **21**, 259–287.

BRUNO, R. & CARBONE, V. 2005 The solar wind as a turbulence laboratory. *Living Rev. Sol. Phys.* **2**, 1–208.

BYCHENKOV, V.Y., SILIN, V.P. & URYUPIN, S.A. 1988 Ion-acoustic turbulence and anomalous transport. *Phys. Rep.* **164**, 119–215.

CARTER, T.A., JI, H., TRINTCHOUK, F., YAMADA, M. & KULSRUD, R.M. 2001 Measurement of lower-hybrid drift turbulence in a reconnecting current sheet. *Phys. Rev. Lett.* **88**, 015001.

CASSAK, P.A., LIU, Y.-H. & SHAY, M.A. 2017 A review of the 0.1 reconnection rate problem. *J. Plasma Phys.* **83**, 715830501.

https://doi.org/10.1017/S002237782510113X Published online by Cambridge University Press

CHE, H., DRAKE, J.F. & SWISDAK, M. 2011 A current filamentation mechanism for breaking magnetic field lines during reconnection. *Nature* **474**, 184–187.

CHEN, L.J. *et al.* 2008 Observation of energetic electrons within magnetic islands. *Nat. Phys.* **4**, 19–23.

CHEN, L.-J. *et al.* 2020 Lower-hybrid drift waves driving electron nongyrotropic heating and vortical flows in a magnetic reconnection layer. *Phys. Rev. Lett.* **125**, 025103.

CHEN, C.H.K. 2016 Recent progress in astrophysical plasma turbulence from solar wind observations. *J. Plasma Phys.* **82**, 535820602.

CHEN, Y., FUJIMOTO, K., XIAO, C. & JI, H. 2015 Plasma waves around separatrix in collisionless magnetic reconnection with weak guide field. *J. Geophys. Res.: Space Phys.* **120**, 6309–6319.

COPPI, B. & FRIEDLAND, A.B. 1971 Processes of magnetic-energy conversion and solar flares. *Astrophys. J.* **169**, 379.

CORONITI, F.V. & EVIATAR, A. 1977 Magnetic field reconnection in a collisionless plasma. *Astrophys. J. Suppl. Ser.* **33**, 189.

COZZANI, G., KHOTYAINTSEV, Y.V., GRAHAM, D.B. & ANDRÉ, M. 2023 Direct observations of electron firehose fluctuations in the magnetic reconnection outflow. *J. Geophys. Res.: Space Phys.* **128**, 1–21.

DAUGHTON, W. 2003 Electromagnetic properties of the lower-hybrid drift instability in a thin current sheet. *Phys. Plasmas* **10**, 3103–3119.

DAUGHTON, W., LAPENTA, G. & RICCI, P. 2004 Nonlinear evolution of the lower-hybrid drift instability in a current sheet. *Phys. Rev. Lett.* **93**, 105004.

DAUGHTON, W., ROYTERSHTEYN, V., ALBRIGHT, B.J., KARIMABADI, H., YIN, L. & BOWERS, K.J. 2009 Influence of coulomb collisions on the structure of reconnection layers. *Phys. Plasmas* **16**, 072117.

DENG, X.H. & MATSUMOTO, H. 2001 Rapid magnetic reconnection in the earth's magnetosphere mediated by whistler waves. *Nature* **410**, 557–560.

DIVIN, A., LAPENTA, G., MARKIDIS, S., NEWMAN, D.L. & GOLDMAN, M.V. 2012 Numerical simulations of separatrix instabilities in collisionless magnetic reconnection. *Phys. Plasmas* **19**, 042110.

DOKGO, K., HWANG, K.-J., BURCH, J.L., CHOI, E., YOON, P.H., SIBECK, D.G. & GRAHAM, D.B. 2019 High-frequency wave generation in magnetotail reconnection: nonlinear harmonics of upper hybrid waves. *Geophys. Res. Lett.* **46**, 7873–7882.

DRAKE, J.F., SWISDAK, M., CATTELL, C., SHAY, M.A., ROGERS, B.N. & ZEILER, A. 2003 Formation of electron holes and particle energization during magnetic reconnection. *Science* **299**, 873–877.

EASTWOOD, J.P., PHAN, T.D., BALE, S.D. & TJULIN, A. 2009 Observations of turbulence generated by magnetic reconnection. *Phys. Rev. Lett.* **102**, 035001.

ERKAEV, N.V., SEMENOV, V.S. & JAMITZKY, F. 2000 Reconnection rate for the inhomogeneous resistivity petschek model. *Phys. Rev. Lett.* **84**, 1455–1458.

FARRELL, W.M., DESCH, M.D., KAISER, M.L. & GOETZ, K. 2002 The dominance of electron plasma waves near a reconnection x-line region. *Geophys. Res. Lett.* **29**, 1–4.

FERMO, R.L., DRAKE, J.F. & SWISDAK, M. 2012 Secondary magnetic islands generated by the Kelvin–Helmholtz instability in a reconnecting current sheet. *Phys. Rev. Lett.* **108**, 255005.

FITZPATRICK, R. 2016 Current-driven ion acoustic instability. Available at: https://farside.ph.utexas.edu/teaching/plasma/Plasma/node119.html. [Accessed 22–01–2025].

FONSECA, R.A. *et al.* 2002 Osiris: A three-dimensional, fully relativistic particle in cell code for modeling plasma based accelerators. *Proc. Int. Conf. Comput. Sci.* **2331**, 342–351.

FORBES, T.G. 1991 Magnetic reconnection in solar flares. *Geophys. Astrophys. Fluid Dyn.* **62**, 15–36.

FOX, N.J. *et al.* 2015 The solar probe plus mission: humanity's first visit to our star. *Space Sci. Rev.* **204**, 7–48.

FRIED, B.D. & GOULD, R.W. 1961 Longitudinal ion oscillations in a hot plasma. *Phys. Fluids* **4**, 139–147.

FRISCH, U. 1995 *Turbulence: The Legacy of A.N. Kolmogorov*. Cambridge University Press.

FUJIMOTO, K. 2014 Wave activities in separatrix regions of magnetic reconnection. *Geophys. Res. Lett.* **41**, 2721–2728.

GALEEV, A.A. & SAGDEEV, R.Z. 1983 Wave-particle interaction. In *Basic Plasma Physics: Selected Chapters, Handbook of Plasma Physics*, vol. 1, p. 389.

https://doi.org/10.1017/S002237782510113X Published online by Cambridge University Press

GOSLING, J.T., BIRN, J. & HESSE, M. 1995 Three-dimensional magnetic reconnection and the magnetic topology of coronal mass ejection events. *Geophys. Res. Lett.* **22**, 869–872.

GRAHAM, D.B. *et al.* 2017 Lower hybrid waves in the ion diffusion and magnetospheric inflow regions. *J. Geophys. Res.: Space Phys.* **122**, 517–533.

GRAHAM, D.B. *et al.* 2019 Universality of lower hybrid waves at earth's magnetopause. *J. Geophys. Res.: Space Phys.* **124**, 8727–8760.

GRAHAM, D.B. *et al.* 2021 Kinetic electrostatic waves and their association with current structures in the solar wind. *Astron. Astrophys.* **656**, A23.

GRAHAM, D.B. *et al.* 2022 Direct observations of anomalous resistivity and diffusion in collisionless plasma. *Nat. Commun.* **13**, 1–9.

GURNETT, D.A. & ANDERSON, R.R. 1977 Plasma wave electric fields in the solar wind: initial results from helios 1. *J. Geophys. Res.* **82**, 632–650.

GURNETT, D.A. & FRANK, L.A. 1978 Ion acoustic waves in the solar wind. *J. Geophys. Res.: Space Phys.* **83**, 58–74.

HALEKAS, J.S. *et al.* 2020 Electrons in the young solar wind: first results from the parker solar probe. *Astrophys. J. Supplem. Ser.* **246**, 22.

HARE, J.D. *et al.* 2018 An experimental platform for pulsed-power driven magnetic reconnection. *Phys. Plasmas* **25**, 055703.

HARRIS, E.G. 1962 On a plasma sheath separating regions of oppositely directed magnetic field. *Il Nuovo Cimento* **23**, 115–121, 1955.

HELLINGER, P., TRÁVNÍČEK, P. & MENIETTI, J.D. 2004 Effective collision frequency due to ion-acoustic instability: theory and simulations. *Geophys. Res. Lett.* **31**, 1–4.

HELLINGER, P., TRÁVNÍČEK, P.M., ŠTVERÁK, ŠTĚPÁN, MATTEINI, L. & VELLI, M. 2013 Proton thermal energetics in the solar wind: helios reloaded. *J. Geophys. Res.: Space Phys.* **118**, 1351–1365.

HEMKER, R.G. 2015 Particle-in-cell modeling of plasma-based accelerators in two and three dimensions. [Online]. Available at: http://arxiv.org/abs/1503.00276.

HESSE, M. *et al.* 2018 On the role of separatrix instabilities in heating the reconnection outflow region. *Phys. Plasmas* **25**, 122902.

HESSE, M. & CASSAK, P.A. 2020 Magnetic reconnection in the space sciences: past, present, and future. *J. Geophys. Res.: Space Phys.* **125**, 1–24.

JARA-ALMONTE, J., DAUGHTON, W. & JI, H. 2014 Debye scale turbulence within the electron diffusion layer during magnetic reconnection. *Phys. Plasmas* **21**, 032114.

JI, H., DAUGHTON, W., JARA-ALMONTE, J., LE, A., STANIER, A. & YOO, J. 2022 Magnetic reconnection in the era of exascale computing and multiscale experiments. *Nat. Rev. Phys.* **4**, 263–282.

JI, H., YAMADA, M., HSU, S. & KULSRUD, R. 1998 Experimental test of the Sweet–Parker model of magnetic reconnection. *Phys. Rev. Lett.* **80**, 3256–3259.

KADOMTSEV, B.B. & PETVIASHVILI, V.I. 1962 Turbulence of a plasma situated in a magnetic field. *Sov. Phys. JETP* **43**, 2234.

KHOTYAINTSEV, Y.V., GRAHAM, D.B., NORGREN, C. & VAIVADS, A. 2019 Collisionless magnetic reconnection and waves: progress review. *Front. Astron. Space Sci.* **6**, 1–20.

KULSRUD, R.M. 1998 Magnetic reconnection in a magnetohydrodynamic plasma. *Phys. Plasmas* **5**, 1599–1606.

KULSRUD, R.M. 2014 Magnetic reconnection: Sweet–Parker versus petschek. *Earth, Planets Space* **53**, 417–422.

LABELLE, J. & TREUMANN, R.A. 1988 Plasma waves at the dayside magnetopause. *Space Sci. Rev.* **47**, 1–2.

LAITINEN, T.V., KHOTYAINTSEV, Y.V., ANDRÉ, M., VAIVADS, A. & RÈME, H. 2010 Local influence of magnetosheath plasma beta fluctuations on magnetopause reconnection. *Ann. Geophys.* **28**, 1053–1063.

LAPENTA, G., MARKIDIS, S., DIVIN, A., NEWMAN, D. & GOLDMAN, M. 2014 Separatrices: the crux of reconnection. *J. Plasma Phys.* **81**, 325810109.

LE, A., DAUGHTON, W., CHEN, L.J. & EGEDAL, J. 2017 Enhanced electron mixing and heating in 3-D asymmetric reconnection at the Earth's magnetopause. *Geophys. Res. Lett.* **44**, 2096–2104.

https://doi.org/10.1017/S002237782510113X Published online by Cambridge University Press

LE, A., DAUGHTON, W., OHIA, O., CHEN, L.-J., LIU, Y.-H., WANG, S., NYSTROM, W.D. & BIRD, R. 2018 Drift turbulence, particle transport, and anomalous dissipation at the reconnecting magnetopause. *Phys. Plasmas* **25**, 062103.

LE, A., STANIER, A., DAUGHTON, W., NG, J., EGEDAL, J., NYSTROM, W.D. & BIRD, R.2019 Three-dimensional stability of current sheets supported by electron pressure anisotropy. *Phys. Plasmas* **26**, 102114.

LIU, Y.H., CASSAK, P., LI, X., HESSE, M., LIN, S.C. & GENESTRETI, K. 2022 First-principles theory of the rate of magnetic reconnection in magnetospheric and solar plasmas. *Commun. Phys.* **5**, 1–9.

LIU, Z., SILVA, C., MILANESE, L.M., ZHOU, M., MANDELL, N.R. & LOUREIRO, N.F. 2025 Electron-only magnetic reconnection and inverse magnetic-energy transfer at subion scales. *Phys. Rev. Lett.* **134**, 155201.

LIU, Z., WHITE, R., FRANCISQUEZ, M., MILANESE, L.M. & LOUREIRO, N.F. 2024 A two-dimensional numerical study of ion-acoustic turbulence. *J. Plasma Phys.* **90**, 965900101.

LOUREIRO, N.F. & BOLDYREV, S. 2017 Role of magnetic reconnection in magnetohydrodynamic turbulence. *Phys. Rev. Lett.* **118**, 245101.

MATSUMOTO, H., DENG, X.H., KOJIMA, H. & ANDERSON, R.R. 2003 Observation of electrostatic solitary waves associated with reconnection on the dayside magnetopause boundary. *Geophys. Res. Lett.* **30**, 1–4.

MOZER, F.S., AGAPITOV, O.V., KASPER, J.C., LIVI, R., ROMEO, O. & VASKO, I.Y. 2023 Direct observation of solar wind proton heating from in situ plasma measurements. *Astron. Astrophys.* **673**, L3.

MÜLLER, D., MARSDEN, R.G., ST. CYR, O.C. & GILBERT, H.R. 2012 Solar orbiter: exploring the sun–heliosphere connection. *Sol. Phys.* **285**, 25–70.

NG, J., CHEN, L.-J., LE, A., STANIER, A., WANG, S. & BESSHO, N. 2020*a* Lower-hybrid-drift vortices in the electron-scale magnetic reconnection layer. *Geophys. Res. Lett.* **47**, 1–8.

NG, J., HAKIM, A., WANG, L. & BHATTACHARJEE, A. 2020*b* An improved ten-moment closure for reconnection and instabilities. *Phys. Plasmas* **27**, 082106.

OSMAN, K.T., MATTHAEUS, W.H., GOSLING, J.T., GRECO, A., SERVIDIO, S., HNAT, B., CHAPMAN, S.C. & PHAN, T.D. 2014 Magnetic reconnection and intermittent turbulence in the solar wind. *Phys. Rev. Lett.* **112**, 215002.

PETKAKI, P., FREEMAN, M.P., KIRK, T., WATT, C.E.J. & HORNE, R.B. 2006 Anomalous resistivity and the nonlinear evolution of the ion-acoustic instability. *J. Geophys. Res.: Space Phys.* **111**, 1–12.

PETKAKI, P., WATT, C.E.J., HORNE, R.B. & FREEMAN, M.P. 2003 Anomalous resistivity in non-maxwellian plasmas. *J. Geophys. Res.: Space Phys.* **108**, 1–11.

PETSCHEK, H.E.1964 Magnetic field annihilation. In *AAS NASA Symposium on the Physics of Solar Flares: Proceedings of a Symposium Held at the Goddard Space Flight Center, Greenbelt, Maryland, October 28–30, 1963*, vol. 50, p. 425. National Aeronautics and Space Administration.

PETVIASHVILI, V.I. 1963 Ion-sonic oscillations generated by electron current. *Dokl. Akad. Nauk.* **153**, 1295–1298.

PHAN, T.D. *et al.* 2018 Electron magnetic reconnection without ion coupling in earth's turbulent magnetosheath. *Nature* **557**, 202–206.

PÍŠA, D. *et al.* 2021 First-year ion-acoustic wave observations in the solar wind by the rpw/tds instrument on board solar orbiter. *Astron. Astrophys.* **656**, A14.

RETINÒ, A., SUNDKVIST, D., VAIVADS, A., MOZER, F., ANDRÉ, M. & OWEN, C.J. 2007 In situ evidence of magnetic reconnection in turbulent plasma. *Nat. Phys.* **3**, 235–238.

RICCI, P., BRACKBILL, J.U., DAUGHTON, W. & LAPENTA, G. 2004 Influence of the lower hybrid drift instability on the onset of magnetic reconnection. *Phys. Plasmas* **11**, 4489–4500.

RICHARDSON, J.D. & SMITH, C.W. 2003 The radial temperature profile of the solar wind. *Geophys. Res. Lett.* **30**, 1–3.

ROYTERSHTEYN, V., DAUGHTON, W., KARIMABADI, H. & MOZER, F.S. 2012 Influence of the lower-hybrid drift instability on magnetic reconnection in asymmetric configurations. *Phys. Rev. Lett.* **108**, 185001.

RUDAKOV, L.I. & KORABLEV, L.V. 1966 Quasilinear theory of current instability in a plasma. *Zh. éksp. Teor. Fiz* **50**, 145–152.

https://doi.org/10.1017/S002237782510113X Published online by Cambridge University Press

SAGDEEV, R.Z. 1967 On ohm's law resulting from instability. In *Proceedings of Symposia in Applied Mathematics*, pp. 281–286.

SAGDEEV, R.Z. 1979 The 1976 oppenheimer lectures: critical problems in plasma astrophysics. i. turbulence and nonlinear waves. *Rev. Mod. Phys.* **51**, 1–9.

SAVITZKY, A. & GOLAY, M.J.E. 1964 Smoothing and differentiation of data by simplified least squares procedures. *Anal. Chem.* **36**, 1627–1639.

SCHINDLER, K. 2006 *Physics of Space Plasma Activity*. Cambridge University Press.

SCHOLER, M. & ROTH, D. 1987 A simulation study on reconnection and small-scale plasmoid formation. *J. Geophys. Res.: Space Phys.* **92**, 3223–3233.

SERVIDIO, S., DMITRUK, P., GRECO, A., WAN, M., DONATO, S., CASSAK, P.A., SHAY, M.A., CARBONE, V. & MATTHAEUS, W.H. 2011 Magnetic reconnection as an element of turbulence. *Nonlinear Proc. Geophys.* **18**, 675–695.

SERVIDIO, S., MATTHAEUS, W.H., SHAY, M.A., CASSAK, P.A. & DMITRUK, P. 2009 Magnetic reconnection in two-dimensional magnetohydrodynamic turbulence. *Phys. Rev. Lett.* **102**, 115003.

SHAY, M.A. & DRAKE, J.F. 1998 The role of electron dissipation on the rate of collisionless magnetic reconnection. *Geophys. Res. Lett.* **25**, 3759–3762.

SLAVIN, J.A. *et al.* 2009 Messenger observations of magnetic reconnection in mercury's magnetosphere. *Science* **324**, 606–610.

SMITH, E., MARSDEN, R. & PAGE, D. 1995 Ulysses above the sun's south pole: an introduction. *Science* **268**, 1005–1007.

SMITH, D.F. & PRIEST, E.R. 1972 Current limitation in solar flares. *Astrophys. J.* **176**, 487.

SORRISO-VALVO, L., MARINO, R., CARBONE, V., NOULLEZ, A., LEPRETI, F., VELTRI, P., BRUNO, R., BAVASSANO, B. & PIETROPAOLO, E. 2007 Observation of inertial energy cascade in interplanetary space plasma. *Phys. Rev. Lett.* **99**.

TREUMANN, R.A. 2014 Origin of resistivity in reconnection. *Earth, Planets Space* **53**, 453–462.

TU, C.Y. & MARSCH, E. 1995 Mhd structures, waves and turbulence in the solar wind: observations and theories. *Space Sci. Rev.* **73**, 1–210.

UGAI, M. & TSUDA, T. 1977 Magnetic field-line reconnexion by localized enhancement of resistivity: part 1. evolution in a compressible mhd fluid. *J. Plasma Phys.* **17**, 337–356.

UZDENSKY, D.A. 2003 Petschek-like reconnection with current-driven anomalous resistivity and its application to solar flares. *Astrophys. J.* **587**, 450–457.

UZDENSKY, D.A. 2011 Magnetic reconnection in extreme astrophysical environments. *Space Sci. Rev.* **160**, 45–71.

VERSCHAREN, D., KLEIN, K.G. & MARUCA, B.A. 2019 The multi-scale nature of the solar wind. *Living Rev. Sol. Phys.* **16**, 1–136.

WANG, S. *et al.* 2022 Lower-hybrid wave structures and interactions with electrons observed in magnetotail reconnection diffusion regions. *J. Geophys. Res.: Space Phys.* **127**, 1–23.

WANG, S., CHEN, L.-J., NG, J., BESSHO, N. & HESSE, M. 2021 Lower-hybrid drift waves and their interaction with plasmas in a 3d symmetric reconnection simulation with zero guide field. *Phys. Plasmas* **28**, 072102.

WATT, C.E.J., HORNE, R.B. & FREEMAN, M.P. 2002 Ion-acoustic resistivity in plasmas with similar ion and electron temperatures. *Geophys. Res. Lett.* **29**, 1–4.

WEYGAND, J.M., MATTHAEUS, W.H., DASSO, S. & KIVELSON, M.G. 2011 Correlation and taylor scale variability in the interplanetary magnetic field fluctuations as a function of solar wind speed: correlation and taylor scale in the imf. *J. Geophys. Res.: Space Phys.* **116**, 1–12.

WEYGAND, J.M., MATTHAEUS, W.H., DASSO, S., KIVELSON, M.G., KISTLER, L.M. & MOUIKIS, C. 2009 Anisotropy of the taylor scale and the correlation scale in plasma sheet and solar wind magnetic field fluctuations. *J. Geophys. Res.: Space Phys.* **114**, 1–15.

WILSON, L.B., III, STEVENS, M.L., KASPER, J.C., KLEIN, K.G., MARUCA, B.A., BALE, S.D., BOWEN, T.A., PULUPA, M.P., SALEM, C. & S 2018 The statistical properties of solar wind temperature parameters near 1 au. *Astrophys. J. Supplem. Ser.* **236**, 41.

WINARTO, H.W. & KUNZ, M.W. 2022 Triggering tearing in a forming current sheet with the mirror instability. *J. Plasma Phys.* **88**, 905880210.

YAMADA, M., KULSRUD, R. & JI, H. 2010 Magnetic reconnection. *Rev. Mod. Phys.* **82**, 603–664.

https://doi.org/10.1017/S002237782510113X Published online by Cambridge University Press

YAMADA, M., LEVINTON, F.M., POMPHREY, N., BUDNY, R., MANICKAM, J. & NAGAYAMA, Y. 1994 Investigation of magnetic reconnection during a sawtooth crash in a high-temperature tokamak plasma. *Phys. Plasmas* **1**, 3269–3276.

YI, Y., PANG, Y., SONG, L., JIN, R. & DENG, X. 2023 Particle-in-cell simulation of energy conversion at the turbulent region downstream of the reconnection front. *Astrophys. J.* **946**, 112.

YOO, J. *et al.* 2020 Lower hybrid drift waves during guide field reconnection. *Geophys. Res. Lett.* **47**, 1–10.

ZHANG, S. *et al.* 2023 Ion and electron acoustic bursts during anti-parallel magnetic reconnection driven by lasers. *Nat. Phys.* **19**, 909–916.

ZHOU, M., LIU, Z. & LOUREIRO, N.F. 2023 Spectrum of kinetic-alfvén-wave turbulence: intermittency or tearing mediation? *Mon. Not. R. Astron. Soc.* **524**, 5468–5476.

ŠTVERÁK, Š., TRÁVNÍČEK, P.M. & HELLINGER, P. 2015 Electron energetics in the expanding solar wind via Helios observations. *J. Geophys. Res.: Space Phys.* **120**, 8177–8193.

https://doi.org/10.1017/S002237782510113X Published online by Cambridge University Press